ANNUAL REPORT 2007

GEORGIA TECH FUSION RESEARCH CENTER

A. INTERPRETATION OF EDGE PEDESTAL ROTATION MEASUREMENTS IN DIII-D

W. M. Stacey, Georgia Tech and R. J. Groebner, General Atomics

Abstract

A methodology for inferring experimental toroidal angular momentum transfer rates from measured toroidal rotation velocities and other measured quantities has been developed and applied to analyze rotation measurements in the DIII-D edge pedestal. The experimentally inferred values have been compared with predictions based on atomic physics processes and on neoclassical toroidal viscosity. The poloidal rotation velocities have been calculated, from poloidal momentum balance using neoclassical parallel viscosity, and compared with measured values in the DIII-D edge pedestal.

Introduction

There is a long-standing research interest in the steep-gradient edge pedestal region (e.g. Refs. 1-4) of high confinement (H-mode) tokamaks, stimulated at least in part by predictions[5,6] that, because of the "stiffness" observed in core plasma temperature profiles, the achievable central temperatures and densities in future tokamaks will be sensitive to the values of the temperature and density at the top of the edge pedestal. We previously have shown[7,8] that momentum balance determines a requirement on the main ion pressure gradient $L_{pi}^{-1} \equiv -\left(\partial p_i/\partial r\right)/\, p_i = \left(V_{ri} - V_{pinchi}\right)\big/ D_i$, where V_{ri} is the radial particle velocity that must satisfy the continuity equation, V_{pinchi} is a collection of terms involving the poloidal and toroidal rotation velocities and other terms (radial and toroidal electric field, beam momentum input), and D_i is a diffusion coefficient type term involving interspecies and viscous momentum transfer frequencies. It was found[8] that the pinch term (hence the rotation velocities and the radial electric field) dominated the determination of the edge pressure gradient in several DIII-D shots. Thus, the next question is what causes the structure in the rotation velocity profiles in the edge pedestal which in turn cause the structure in the density and pressure profiles in the edge pedestal. Thus motivated, we have undertaken a study of rotation velocities measured in the DIII-D edge pedestal

Rotation Measurements and Analysis

Discharge 119436 was run in a lower single null divertor (SND) configuration with plasma current I_p=1.0 MA, toroidal field B_t = 1.6 T and average triangularity δ = 0.35. During the time of interest (3.0-3.5 s), the injected beam power P_{beam} was 4.3 MW, the line-averaged density $<n_e>$ was about 0.34 x10^{20} m^{-3}, the global stored energy W_{MHD} was about 0.55 MJ and the average ELM (edge localized mode) period was 15.3 ms. Even though the global parameters, such as $<n_e>$ and W_{MHD}, were approximately constant during the time of interest, the conditions in the pedestal were constantly changing due to the effect of ELMs. The period 80-99% between ELMs was chosen for analysis for this shot.

Discharge 98889 was also run in a lower SND configuration with I_p=1.2 MA, toroidal field B_t = 2.0 T and average δ = 0.07. During the time of interest (3.75-4.11 s), P_{beam} was 3.1 MW, $<n_e>$ was about 0.40 x10^{20} m^{-3}, W_{MHD} was about 0.59 MJ and the average ELM period was 36.0 ms. Similarly to discharge 119436, the maximum electron pressure gradient varied by at least a factor of 2-3 during an ELM cycle, even though the global parameters were roughly constant during the time of interest. The period 40-60% between ELMs was chosen for analysis for this shot.

Discharge 118897 was also a lower SND configuration with I_p = 1.4 MA, toroidal field B_t = 2.0 T and average δ = 0.4. At the time of interest (2.14 s), the plasma was in a well-developed ELM-free H-mode stage with slowly varying parameters P_{beam} = 2.35 MW, $<n_e>$ = 7.7 x10^{19} m^{-3} and W_{MHD} = 0.68 MJ.

Composite density and temperature profiles, for use in the transport calculations, were obtained by data from appropriate time bins during the time of interest in these discharges. For the ELMing shots 119436 and 98889, this process began with the use of an algorithm to determine the start and end time of each ELM, from filtering of a D_α signal. Then, the interval between adjacent ELMs was sub-divided into typically 5 time intervals for purposes of binning the data. These intervals were chosen to be some fraction of the time between the ELMs (10-20%, 20-40%, 40-60%, 60-80% and 80-99%). These temperature and density data data were then averaged within each bin and fit.

An integrated modeling code[9] was used to supplement the experimental data. This code i) calculated particle and power balances on the core plasma to determine the net particle and heat outfluxes from the core into the scrape-off layer (SOL), calculated using measured confinement times, which were input to ii) an extended 2-point divertor plasma model (with radiation and atomic physics) that calculated densities and temperatures in the SOL and divertor and the ion flux incident on the divertor plate, which iii) was recycled as neutral atoms and molecules that were transported through the 2D divertor region across the separatrix to fuel the core plasma.

Rotation Theory

Toroidal

The analysis in this work was based on particle and momentum balance. For the purpose of interpreting measured rotation velocities, it is useful to write the toroidal momentum balance equation in terms of angular momentum transport rates $Rn_j m_j \nu_{xj} \upsilon_{\phi j}$ associated with various processes "x (e.g. charge-exchange, viscosity, anomalous torque), in which case the FSA toroidal angular momentum balance equation for plasma species "j" can quite generally be written

$$n_j m_j [\nu_{jk} \left(\upsilon_{\phi j} - \upsilon_{\phi k} \right) + \nu_{dj} \upsilon_{\phi j}] = n_j e_j E_\phi^A + e_j B_\theta \Gamma_{rj} + M_{\phi j} \qquad (1)$$

where ν_{dj} represents the total toroidal angular momentum transfer frequency due to neoclassical and anomalous viscosity (or torques), convection, atomic physics and other processes (e.g. field ripple) that can be written in the $Rn_j m_j \nu_{xj} \upsilon_{\phi j}$ form $\left(\nu_{dj} = \nu_{dj}^{visc} + \nu_{dj}^{inert} + \nu_{dj}^{atom} + \nu_{dj}^{anom} \right)$, ν_{jk} is the interspecies collision frequency (a sum over all other species $k \neq j$ is implied), E_ϕ^A is the electromagnetically induced toroidal electric field, $\Gamma_{rj} \equiv n_j \upsilon_{rj}$ is the radial particle flux determined by solution of the continuity equation, and $M_{\phi j}$ is the toroidal component of the momentum input (e.g. by neutral beams).

The novel approach that we pursue in this work is to use the measured rotation velocities as input in "solving the equations backwards" to infer the local momentum transport frequency from the toroidal angular momentum equation. Equation (1) for each species can readily be rearranged to yield (for the two-ion-species model) a requirement on the composite angular

momentum transport frequency for all mechanisms (classical and anomalous viscosity, inertial, atomic physics, etc.) that must be satisfied in order to produced the measured rotation velocities

$$\nu_{dj} = \nu_{jk}\left[\frac{n_j e_j E_\phi^A + e_j B_\theta \Gamma_{rj} + M_{\phi j}}{n_j m_j \nu_{jk} \upsilon_{\phi j}} - \left(1 - \frac{\upsilon_{\phi k}}{\upsilon_{\phi j}}\right)\right] \tag{2}$$

(and a similar expression with the "j" and "k" subscripts interchanged). All quantities on the right except the rotation velocities readily can be determined from measurements and solving the continuity equation. Thus, if the toroidal rotation velocities for both ion species are also measured, the momentum transfer frequencies for both species can be determined from Eq. (2) (plus the same equation with "j" and "k" interchanged).

An immediate problem arises because it is not presently possible to measure the rotation velocity for deuterium, the usual main ion species. To get around this problem, we use a perturbation analysis of the above toroidal momentum balance equations for a two-species (deuterium "j", carbon impurity "k") plasma.

First, the toroidal momentum balance Eqs. (1) for the two species are added to eliminate the friction terms and used to define an effective momentum transfer frequency

$$\nu_d^{eff} \equiv \frac{n_j n_j \nu_{dj} + n_k m_k \nu_{dk}}{n_j m_j + n_k m_k} = \frac{\left(n_j e_j E_\phi^A + e_j B_\theta \Gamma_{rj} + M_{\phi j}\right) + \left(n_k e_k E_\phi^A + e_k B_\theta \Gamma_{rk} + M_{\phi k}\right) - \{n_j m_j \nu_{dj}\left(\upsilon_{\phi j} - \upsilon_{\phi k}\right)\}}{(n_j m_j + n_k m_k)\upsilon_{\phi k}} \tag{3}$$

The { } term involving the difference in toroidal velocities is set to zero to obtain a zeroth order approximation of the effective momentum transport frequency, ν_d^0,

$$\nu_d^0 = \frac{\left(n_j e_j E_\phi^A + e_j B_\theta \Gamma_{rj} + M_{\phi j}\right) + \left(n_k e_k E_\phi^A + e_k B_\theta \Gamma_{rk} + M_{\phi k}\right)}{(n_j m_j + n_k m_k)\upsilon_{\phi k}^{\exp}} \tag{4}$$

which is used, along with the measured carbon toroidal velocity, $\upsilon_{\phi k}^{\exp}$, in Eq. (1) for the deuterium "j" species to obtain a zeroth order approximation for the deuterium-carbon velocity difference

$$\left(\upsilon_{\phi j} - \upsilon_{\phi k}\right)_0 = \frac{\left(n_j e_j E_\phi^A + e_j B_\theta \Gamma_{rj} + M_{\phi j}\right) - n_j m_j \nu_d^0 \upsilon_{\phi k}^{\exp}}{n_j m_j \left(\nu_{jk} + \nu_d^0\right)} \tag{5}$$

which in turn is used in Eq. (1) for the carbon impurity "k" species to solve for the carbon momentum transport frequency

$$\nu_{dk} = \frac{\left(n_k e_k E_\phi^A + e_k B_\theta \Gamma_{rk} + M_{\phi k}\right) + n_k m_k \nu_{kj}\left(\upsilon_{\phi j} - \upsilon_{\phi k}\right)_0}{n_k m_k \upsilon_{\phi k}^{\exp}} \tag{6}$$

The deuterium momentum transfer frequency is then calculated from the definition of Eq. (3) using $\nu_d^{eff} \approx \nu_d^0$, which yields $\nu_{dj} \approx \nu_d^0$.

Poloidal

The poloidal rotation is governed by the poloidal component of the momentum balance equation

$$\begin{aligned} &n_j m_j \left[\left(\mathbf{\upsilon}_\mathrm{j} \bullet \nabla\right)\mathbf{\upsilon}_\mathrm{j}\right]_\theta + \left[\nabla \bullet \Pi_\mathrm{j}\right]_\theta + \frac{1}{r}\frac{\partial p_j}{\partial \theta} - M_{\theta j} + n_j m_j \nu_{jk}\left(\upsilon_{\theta j} - \upsilon_{\theta k}\right) + \\ &n_j e_j \left(\upsilon_{rj} B_\phi - E_\theta\right) + n_j m_j \nu_{ionj} \upsilon_{\theta j} + n_j m_j \nu_{elcxj} \upsilon_{\theta j} = 0 \end{aligned} \tag{7}$$

where the a neoclassical parallel viscous force will be written as

$$\left\langle \mathbf{B} \bullet \nabla \bullet \Pi_\parallel^\mathrm{j} \right\rangle_{neo} = \frac{3}{2}\left\langle \eta_{0j} A_{0j}^\theta \frac{\partial B_\theta}{\partial \ell_\theta} \right\rangle \left[\bar{\upsilon}_{\theta j} + \frac{B_\phi K^j T_j L_{Tj}^{-1}}{e_j B^2} \right] + \frac{3}{2}\left\langle \eta_{0j} A_{0j}^\phi \frac{\partial B_\theta}{\partial \ell_\theta} \right\rangle \bar{\upsilon}_{\phi j} \tag{8}$$

where the various quantities are defined in Ref. xx. Representing the poloidal density, velocity and potential asymmetries in the viscous stress tensor[10] A_{0j} with a low order Fourier expansion

$$n_j(r,\theta) \approx n_j^0(r)\left[1 + n_j^c \cos\theta + n_j^s \sin\theta\right] \tag{9}$$

leads to a set of FSA (flux surface averaged) poloidal momentum balance equations, one for each ion species, of the form

$$\begin{aligned} &\hat{\upsilon}_{\theta j}\left[-q\hat{\upsilon}_{\phi j}\,\varepsilon\left(\tilde{n}_j^s + \tilde{\Phi}^s\right) + q^2 f_j f_p\left(1 + \tilde{\Phi}^c + \frac{2}{3}\tilde{n}_j^c\right) + f_p \nu_{jk}^* + f_p \nu_{atj}^*\right] \\ &-\hat{\upsilon}_{\theta k}\nu_{jk}^*\sqrt{\frac{m_j}{m_k}} f_p = -\hat{\upsilon}_{rj} - q\varepsilon\frac{1}{4}\tilde{n}_j^s - q\varepsilon\hat{\Phi}_j\left[\frac{1}{4}\left(\tilde{\Phi}^s\right)\right] + \\ &q^2 f_j f_p\left(\hat{\upsilon}_{\phi j} + \hat{P}_j^i\right)\tilde{\Phi}^c - q\varepsilon\hat{\upsilon}_{\phi j}\left[\left(\hat{\upsilon}_{\phi j} + \hat{P}_j^i\right)\tilde{\Phi}^s + \frac{1}{2}\hat{\upsilon}_{\phi j}\tilde{n}_j^s\right] \end{aligned} \tag{10}$$

where $\varepsilon = r/R, \hat{\upsilon}_{\theta j} = \upsilon_{\theta j} \Big/ f_p \upsilon_{thj}$, $\hat{\upsilon}_{\phi j} = \upsilon_{\phi j} / \upsilon_{thj}, \hat{P}_j^{'} = P_j^{'} \Big/ \upsilon_{thj}, \tilde{n}_j^{s,c} = n_j^{s,c} / \varepsilon$, $f_p \equiv \dfrac{B_\theta}{B_\phi}$, $\hat{\Phi}_j \equiv \dfrac{e_j \Phi^0}{T_j}$.

The atomic physics momentum transfer frequency $\nu_{at} = \nu_{elcx} + \nu_{ion}$ consists of a momentum loss rate due to charge-exchange and elastic scattering term that enters the momentum balance directly plus an ionization term that enters via the inertia terms. The electron momentum balance can be solved for $\tilde{\Phi}^{c/s} \equiv \dfrac{\Phi^{c/s}}{\varepsilon} = \dfrac{n_e^{c/s}}{\varepsilon\left(e\Phi^0 / T_e\right)}$, which represents the poloidal asymmetry in the electrostatic potential. The FSA of the electrostatic potential, Φ^0, is conventionally determined by integrating the radial electric field radially inward from the first grounded (in contact with the vessel) field line. The friction terms are identified by $\nu_{jk}^* = \nu_{jk} qR / \upsilon_{thj}$, and the viscosity terms resulting from the use of the above viscosity expression with coefficient $\eta_{0j} = n_j m_j \upsilon_{thj} qR f_j\left(\nu_{jj}^*\right)$ are identified by $f_j = \dfrac{\varepsilon^{-3/2}\nu_{jj}^*}{\left(1+\varepsilon^{-3/2}\nu_{jj}^*\right)\left(1+\nu_{jj}^*\right)}$ in Eq. (10).

The term

$$\hat{\upsilon}_{rj} \equiv \frac{e_j B_\phi}{m_j \upsilon_{thj}} \frac{qR}{\upsilon_{thj}} \upsilon_{rj} + \frac{f_j q^2 B_\phi}{\upsilon_{thj}} \frac{K^j T_j L_{Tj}^{-1}}{e_j B^2} \tag{11}$$

represents the poloidal rotation driving forces from the VxB force and the heat flux in the parallel viscous force.

The $\tilde{n}^{s,c} = n^{s,c} \big/ \varepsilon$ represent the poloidally asymmetric density components, which can be obtained by solving the equations resulting from taking the $\sin\theta$ and $\cos\theta$ FSA moments of the poloidal momentum balance equation[11].

It is useful at this point to touch base with other solutions for the poloidal rotation velocity in the literature. If we neglect all terms in the FSA poloidal momentum balance equation except the viscous term and neglect the second term on the right in the expression for the parallel viscous force of Eq. (8), we obtain the Hazeltine result[12] $\left[\overline{\upsilon}_\theta^j = -B_\phi K^j T_j L_{Tj}^{-1} \big/ e_j B^2\right]$. If we replaced Eq. (8) with the Hirshman-Sigmar viscous tenso[13] and neglected the inertial terms in the poloidal momentum balance equation we would obtain the equations solved in the NCLASS code[14]. If we replaced Eq. (8) with the Hirshman-Sigmar viscous tensor and retained

only the viscous term in the impurity poloidal momentum balance equation and only the viscous and friction terms in the main ion poloidal momentum balance equation we would obtain the Kim, et al.[15] results for the poloidal rotation. Thus, the above equations include as limiting cases many of the conventional forms of neoclassical theory.

Interpretation of Rotation Measurements

The inferred angular momentum transfer rates for carbon (ν_{dk}) and deuterium ($\nu_{dj} = \nu_d^0$) calculated from Eqs. (6) and (4), respectively, are shown as Cexp and Dexp, repectively, for shot 119436 in Fig. 1. For comparison, the neoclassical gyroviscous momentum transfer frequency[11] for carbon and deuterium are shown also, as is the charge exchange plus elastic scattering plus ionization momentum transfer frequency, Datomic. Similar results were obtained for ELMing H-mode shot 98889 and ELM-free H-mode shot 118897. It is interesting that the inferred momentum transport rates are larger (by about a factor of 5) in the ELMing than in the ELM-free H-mode.

The measured carbon poloidal rotation velocity and the values of the carbon and deuterium velocities calculated from Eqs. (10) are shown for the ELM-free H-mode shot 118897 in Fig. 1. The Shaing-Sigmar parallel viscosity coefficient[16] $\eta_{0j} = n_j m_j \upsilon_{thj} qRf_j\left(\nu_{jj}^*\right)$, with $f_j = \dfrac{\varepsilon^{-3/2}\nu_{jj}^*}{\left(1+\varepsilon^{-3/2}\nu_{jj}^*\right)\left(1+\nu_{jj}^*\right)}$, was used in the calculations. The calculated and measured profiles are similar in magnitude, although they differ in sign at certain radial locations. (Note that the positive sense of the poloidal rotation is taken as the positive poloidal direction in a right-hand ($r-\theta-\phi$) with the positive ϕ direction aligned with the plasma current, which is down at the outboard midplane for these shots). species' velocities are calculated from Eqs. (19), making it difficult to see the latter).

Although the calculated carbon poloidal rotation velocities are in reasonably good agreement with measured values in the flattop region inward of the edge pedestal $\rho \le 0.94$, the calculations clearly fail to predict the (negative) peaking in poloidal velocity in the edge pedestal region.

Summary and Conclusions

A methodology was presented for inferring experimental toroidal angular momentum transfer rates from measured toroidal rotation velocities in the edge pedestal. This methodology was applied to analyze transfer rates of toroidal angular momentum in the edge pedestal of 3 DIII-D H-mode shots. The inferred angular momentum transfer rates are larger than can be explained by atomic physics or neoclassical viscosity.

Calculations of poloidal rotation velocities (based on poloidal momentum balance, using neoclassical parallel viscosity, and taking into account atomic physics) were compared with measured values of the carbon poloidal rotation velocities in the edge pedestal of 3 DIII-D shots. In the "flattop" region in just inside the edge pedestal there was reasonable agreement between calculation and experiment. However, the calculation failed to reproduce the measured structure in the poloidal velocity in the edge pedestal, indicating the presence of some important momentum transport or torque input mechanism in the edge pedestal region that was not accounted for in the calculation.

A novel feature of the poloidal rotation calculation was retention in the poloidal momentum balance of radial particle velocity and poloidal electric field terms usually neglected. Both of these terms were demonstrated to be important in the edge pedestal.

Acknowledgement
Work partially supported by DOE Grant DE-FG02-00-ER54538 with the Georgia Tech Research Corporation for collaboration as a member of the DIII-D National Tokamak Facility Team.

References

1. R. J. Groebner and T. H. Osborne, Phys. Plasmas, 5, 1800 (1998).
2. A. E. Hubbard, R. L. Boivin, R. S. Granetz, et al., Phys. Plasmas, 5, 1744 (1998).
3. W. Suttrop, O. Gruber, B. Kurzan, et al., Plasma Phys. Controlled Fusion, 42, A97 (2000).
4. T. H. Osborne, J. R. Ferron, R. J. Groebner, et al., Plasma Phys. Controlled Fusion, 42, A175 (2000).
5. M. Kotschenreuther, W. Dorland, Q. P. Liu, et al., Proceedings of the 16th Conference on Plasma Physics Controlled Fusion Research, Montreal, 1996 (IAEA, Vienna, 1997), Vol. 2, p 371.

6. J. E. Kinsey, R. E. Waltz and D. P. Schissel, Proceedings of the 24th European Physical Society, Berchtesgarten, 1997, Vol. III, p 1081. Plasma Phys. Controlled Fusion, 42, A97 (2000).
7. W. M. Stacey, Phys. Plasmas, 11, 4295 (2004).
8. W. M. Stacey and R. J. Groebner, Phys. Plasmas, 13, 012513 (2006).
9. W. M. Stacey, Phys. Plasmas, 5, 1015 (1998); 8, 3673 (2001); Nucl. Fusion, 40, 678 (2000).
10. W. M. Stacey, R. W. Johnson and J. Mandrekas, Phys. Plasmas, 13, 062508 (2006).
11. W. M. Stacey, Phys. Plasmas, 9, 3874 (2002).
12. R. D. Hazeltine, Phys. Fluids, 17, 961 (1974).
13. S. P. Hirshman and D. J. Sigmar, Nucl. Fusion, 1079 (1981).
14. W. A. Houlberg, K. C. Shaing, S. P. Hirshman and M. C. Zarnstorff, Phys. Plasmas, 4, 3230 (1997).
15. Y. B. Kim, P. H. Diamond and R. J. Groebner, , Phys. Fluids B, 3, 2050 (1991).
16. W. M. Stacey, A. W. Bailey, D. J. Sigmar and K. C. Shaing, Nucl. Fusion, 25, 463 (1985).

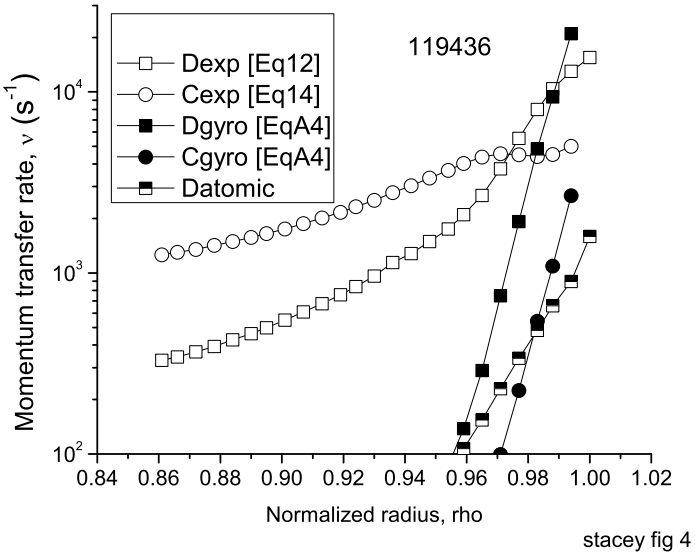

Fig. 1 Experimentally inferred toroidal angular momentum transfer frequency between ELMs in H-mode shot 119436.

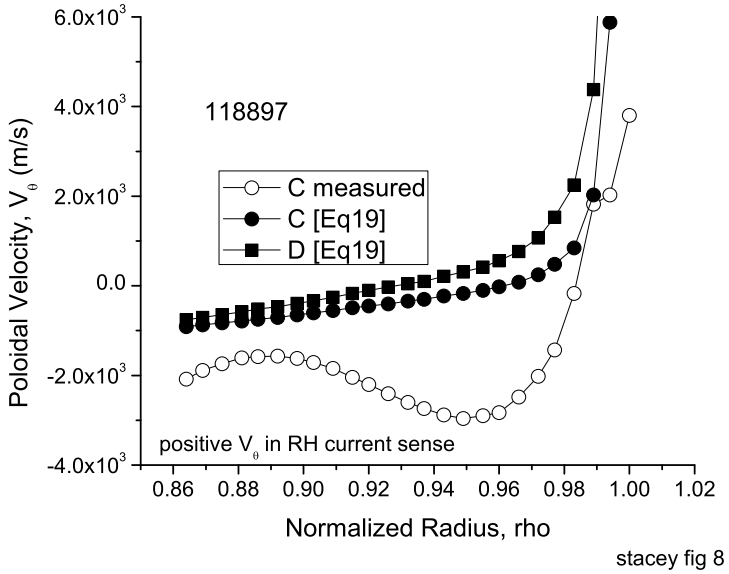

Fig. 2 Poloidal rotation velocities, measured and calculated, in ELM-free H-mode shot 118897.

B. EXPERIMENTALLY INFERRED THERMAL DIFFUSIVITIES IN THE EDGE PEDESTAL BETWEEN ELMS IN DIII-D

W. M. Stacey, Georgia Tech and R. J. Groebner, General Atomics

Abstract

Using temperature and density profiles averaged over the same sub-interval of several successive inter-ELM periods, the ion and electron thermal diffusivities in the edge pedestal were inferred between ELMs (edge localized modes) for two DIII-D discharges. The inference procedure took into account the effects of plasma reheating and density buildup between ELMS, radiation and atomic physics cooling, neutral beam heating and ion-electron equilibration, recycling neutral and beam ionization particle sources in determining the conductive heat flux profiles used to infer the thermal diffusivities in the edge pedestal.

Introduction

The steep-gradient edge pedestal region which forms in H-mode (high confinement) tokamak plasmas has long been a subject of experimental investigation (e.g. Refs. 1-4). This interest stems at least in part from calculations[5,6] that indicate that, because of the "stiffness" observed in core plasma temperature profiles, the achievable central temperatures in future tokamaks will be sensitive to the values of the temperature at the top of the edge pedestal. These pedestal temperature values will depend on the steepness of the temperature gradients in the edge and the width over which the steep gradient region extends inward from the separatrix.

For a given conductive heat flux through the edge, the steepness of the temperature gradient will depend on the thermal diffusivity, which is not known from first principles at this time. This has led to the practice of adjusting thermal (and particle) diffusivities in edge transport simulations to force agreement with measured temperature (and density) profiles in the edge pedestal (e.g. Refs. 7 and 8) in order to determine values for those diffusivities.

We have presented[9] a more systematic and self-consistent procedure for inferring thermal diffusivities in the edge pedestal. This procedure takes into account the effects of radiation and atomic physics cooling, ionization particle sources from recycling neutrals, neutral beam heating, interspecies energy transfer, and convective heat fluxes in determining the conductive heat flux profiles to be used in inferring the thermal diffusivities from the measured temperature profiles.

In our first application[9] of this methodology, we inferred thermal diffusivities from temperature profiles that were "averaged over ELMs" (edge-localized modes). Subsequently, we examined the ELM-free phase of a discharge[10] (in L-mode and H-mode) and an ELM-suppressed discharge[11], and we made an initial investigation[11] of the thermal diffusivity between ELMs. The purpose of this paper is to report the inference of experimental ion and electron thermal diffusivities at different times between ELM crashes for two DIII-D discharges.

Data Analysis

The goal of this study was to examine thermal transport in the H-mode pedestal during the interval between Type I ELMs. For this purpose, discharges were chosen which had globally steady-state conditions for several hundred milliseconds and which had ELMS that were roughly periodic and of the same size during this period. Waveforms for the one of discharges chosen, DIII-D discharge 119436, is shown in Fig. 1. The time of analysis is enclosed between vertical dashed lines in the figure; this time range is 3000-3500 ms for discharge 119436.

Discharge 119436 was run in a lower single null divertor (SND) configuration with plasma current I_p=1.0 MA, toroidal field B_t = 1.6 T and average triangularity δ = 0.35. During the time of interest, the injected beam power P_{beam} was 4.3 MW, the line-averaged density $\langle n_e \rangle$ was about 0.34 x10^{20} m^{-3}, the global stored energy W_{MHD} was about 0.55 MJ and the average ELM period was 15.3 ms. Even though the global parameters, such as $\langle n_e \rangle$ and W_{MHD}, were approximately constant during the time of interest, the conditions in the pedestal were constantly changing due to the effect of ELMs. For instance, the maximum electron pressure gradient varied by at least a factor of 2-3 during an ELM cycle, as shown in the bottom panel of fig. 1a). The smallest absolute values of the pressure gradient occurred just after an ELM crash and the largest before the onset of an ELM.

Composite density and temperature profiles, for use in the transport calculations, were obtained by data from appropriate time bins during the time of interest in these discharges. This process began with the use of an algorithm to determine the start and end time of each ELM, from filtering of a D_α signal. Then, the interval between adjacent ELMs was sub-divided into typically 5 time intervals for purposes of binning the data. These intervals were chosen to be some fraction of the time between the ELMs. For discharge 119436, these bins were chosen to be 10-20%, 20-40%, 40-60%, 60-80% and 80-99% of the ELM cycle. The profiles in each time bin were fit with analytic functions.

The electron temperature T_e and electron density n_e were obtained from a multi-point Thomson scattering system[12]. Prior to the generation of the composite profiles, the Thomson data from each laser pulse were mapped to flux coordinates with an equilibrium fit obtained at the time of the corresponding laser pulse. The mapped T_e and n_e data within each time window were then combined and fit to an analytic function of magnetic flux, which consisted of a tanh function in the pedestal which joined smoothly to a spline fit in the core. After these fits, the T_e and n_e data were adjusted spatially by an amount required to align the foot of the tanh function fit to the T_e profile with the plasma separatrix. These adjustments were typically 1 cm or less in radius at the outer midplane. The density profiles were adjusted to match the line-averaged density from a CO2 density interferometer. These adjustments were typically less than 10%. The ion temperature and carbon density were obtained from measurements of the C VI 5290 line with a charge exchange recombination spectroscopy system[13]. The ion temperature T_i was fit with a spline function and this provided a good fit both in the pedestal region and in the core of the plasma. An absolute intensity calibration was used to convert the intensity measurements of the C VI ions into a carbon density. These densities were used to compute Z_{eff} and the main ion density, under the assumption that carbon is the dominant impurity in the plasma. After all of these profiles were obtained, a total pressure profile was computed, including fast ion pressure from a beam deposition calculation with the ONETWO code[14].

Figure 2 shows data and fits to the data for some of the time bins used in this study for 10-20% and 80-90% of the ELM cycle in discharge 119436. The bin at 10-20% represents the state of the plasma shortly after an ELM crash whereas the bin at 80-99% represents the pedestal just before an ELM crash. These data show that all profiles collapsed at an ELM and re-built prior to the next ELM. This is true also for the T_i profile, which was measured in this discharge with a 0.552 ms resolution. However, these data show that the n_e profile in the outer 1-2% of the confined plasma decreased as the ELM cycle proceeds. This slow decrease may reflect a recovery from changes in the scrape-off layer and associated fuelling due to an ELM.

Time derivatives of the temperature and density fits are required for the time dependent transport analysis performed here. For each of these quantities, the analytic fit in each time bin is evaluated on the transport grid, which is an array of points in flux space. At each grid point, a polynomial of order two is fit as a function of time to the data from the various time bins. After

the fit in time is obtained, the time derivative is evaluated by analytic differentiation of the polynomial fit in each time bin.

Procedure for inference of thermal diffusivities

Expressions for the evaluation of the radial thermal diffusivities from the data of the previous section can be inferred from the radial heat conduction relations for ions and electrons

$$\chi_{i,e}^{\exp}(r) = L_{Ti,e}(r)\frac{q_{i,e}(r)}{n_{i,e}(r)T_{i,e}(r)} \equiv L_{Ti,e}(r)\left[\frac{Q_{i,e}(r)}{n_{i,e}(r)T_{i,e}(r)} - \frac{5}{2}\frac{\Gamma_{i,e}(r)}{n_{i,e}(r)}\right] \qquad (1)$$

where $L_{Ti,e}^{-1} \equiv -\left(\partial T_{i,e}/\partial r\right)/T_{i,e}$, $Q_{i,e}$ are the total heat fluxes, which satisfy

$$\frac{\partial Q_i}{\partial r} = -\frac{\partial}{\partial t}\left(\frac{3}{2}n_i T_i\right) + q_{nbi} - \frac{3}{2}\left(T_i - T_o^c\right)n_i n_o^c \left\langle \sigma v\right\rangle_{cx+el} - q_{ie}\ ,\ Q_i\left(r_{sep}\right) = Q_{sepi}^{\exp} \qquad (2)$$

and

$$\frac{\partial Q_e}{\partial r} = -\frac{\partial}{\partial t}\left(\frac{3}{2}n_e T_e\right) + q_{nbe} + q_{ie} - n_e n_o \left\langle \sigma v\right\rangle_{ion} E_{ion} - n_e n_z L_z\ ,\ Q_e\left(r_{sep}\right) = Q_{sepe}^{\exp} \qquad (3)$$

and $\Gamma_{i,e} \equiv n_{i,e}\upsilon_{ri,e}$ is the radial particle flux, which satisfies

$$\frac{\partial \Gamma_i}{\partial r} = -\frac{\partial n_i}{\partial t} + n_e n_o \left\langle \sigma v\right\rangle_{ion} + S_{nb}\ ,\quad \Gamma_i\left(r_{sep}\right) = \Gamma_{sepi}^{\exp} \qquad (4)$$

In these equations, n_o is the recycling or gas fueling neutral density in the edge pedestal (the superscript "c" denotes uncollided "cold" neutrals), $q_{nbi,e}$ is the neutral beam heating, S_{nb} is the neutral beam particle source, q_{ie} is the collisional energy transfer from ions to electrons, $\left\langle \sigma v\right\rangle_x$ is an atomic physics reaction rate (x=cx+el denotes charge-exchange plus

elastic scattering, x=ion denotes ionization), n_z and L_z are the impurity density and radiation emissivity, and E_{ion} is the ionization potential

The same integrated modeling code[15] discussed in the previous section A was used to calculate the recycling and fueling neutral distributions..

Equations (2)-(4) were solved for the heat and particle flux profiles in the edge pedestal region, using the experimental density and temperature profiles determined for each sub-interval (e.g. 10-20%) in the interval between successive ELM crashes. The separatrix boundary conditions on the particle and heat fluxes were the "steady-state" experimental values determined from the integrated modeling code as described in the previous paragraph but then corrected to account for the reduction in fluxes crossing the separatrix due to reheating and repopulating the pedestal between ELM crashes. In effect, the particle and heat fluxes flowing from the core into the pedestal region were similar over the entire interval between ELM crashes, but the particle and heat outfluxes flowing across the separatrix varied in time because the experimental heating and particle buildup rates did.

The heat and particle fluxes calculated from Eqs. (2)-(4) for each sub-interval between ELM crashes were then used, together with the experimental density and temperature profiles for that sub-interval, to infer the experimental thermal diffusivities from Eq. (1). The resulting heating and particle flux profiles in the pedestal varied over the inter-ELM cycle because the heating and density buildup rates varied and because the neutral influx varied because of the different experimental density profiles used calculations.

Inference of Thermal Diffusivity Between ELMS

The radial heating and cooling rates at 10-20 % after (post ELM) and 80-99% after (pre ELM) the ELM crash are shown for shot 119436 in Figs. 3. The reheating of the pedestal (dW/dt) terms dominated the pedestal power balance shortly after the ELM crash (post ELM), except in the very edge ($\rho > .99$) where charge-exchange (and elastic scattering) cooling was dominant. At a later time just before the next ELM crash (pre ELM) the reheating terms were still the largest terms for $\rho < .95$, but were comparable to the other beam and atomic physics terms; for $\rho > .95$ charge exchange was dominant and the pedestal plasma was actually cooling.

As a consequence of the heat flux from the core being deposited in the pedestal to reheat the plasma, the total heat flux for both ions and electrons actually decreased with radius (shown in Figs. 4), which is quite different from the results found previously[10] for the ELM-free H-mode (heat fluxes increasing with radius). The heat fluxes decreased more sharply with radius just after the ELM crash, when the edge reheating rate was greater, than later just before the next ELM crash.

The inferred thermal diffusivities are given in Figs 5. For the ions, the χ_i is about the same over the period between ELMs in the inner region ($\rho < .92$), but is larger in the region of most intense reheating ($.94 < \rho < .98$) just after the crash than later. The electron χ_e is larger just after the ELM crash than later (which is at odds with what might be expected based on the observed increase in turbulence with time after the ELM crash). In the very edge ($\rho > .99$) both χ_i and χ_e increased with time after the ELM crash (and the gradients become steeper). The inferred χ_e profile and magnitude long after an ELM and just before the next ELM crash (pre-ELM) is similar to what was found previously for an ELM-free H-mode plasma[10], although the inferred χ_i is different in both shape and magnitude (the ELM-free shot had different parameters than shot 119436). The reduction over time of the thermal diffusivity in the spatial region around $\rho \approx .96$ apparently reduces the heat flux into the region $\rho > .96$ sufficiently later in the inter-ELM period to produce the cooling in that region shown in Fig. 3.b.

The overall conclusions suggested by Figs. 3-5 are that both the ion and electron channels are of comparable importance for heat transport through the pedestal between ELMS and that the magnitude of the conductive heat transfer coefficients (thermal diffusivities) tend to decrease somewhat (by less than a factor of 2) with time for both the ions and electrons over the time interval between ELMs. The magnitude and shape of the χ_e profile just before the ELM crash (pre-ELM) are similar to what we found previously for an ELM-free H-mode phase in DIII-D[10], but the χ_i profile is not (we note that the resolution of the T_i data was 10 ms in the previous work, as compared to 0.552 ms in this work, although this should not be too important for the ELM-free discharge).

The same set of calculations was repeated for the data from shot 98889, with similar results.

Summary and Conclusions

The ion and electron thermal diffusivities within different sub-intervals of the time interval between ELM crashes were inferred from experimental measurements of temperature and density profiles and heating rates (dW/dt) in the edge pedestal for 2 DIII-D discharges. The experimental data were averaged over the same sub-intervals of several intra-ELM intervals.

These experimental data were used to solve the power and particle balance equations for the heat and particle fluxes that were then used together with the measured temperature and density profiles to infer the thermal diffusivities. Neutral recycling cooling and particle source effects, radiation cooling, neutral beam heating and particle sources, ion-electron equilibration, and reheating and density buildup effects were taken into account. The plasma reheating between ELMs was a dominant effect over most of the edge region, except in the very edge where charge-exchange was dominant, in the power balance equations, hence in determining the heat flux profiles used in inferring the thermal diffusivities.

The inferred electron thermal diffusivities decreased at most by about a factor of two from the time immediately following an ELM crash to the time just before the next ELM crash, except just inside the separatrix where an opposite trend was inferred. This decrease occurred over the entire edge region for shot 119436, but only over the steep-gradient region around $\rho \approx 0.96$ for shot 98889. A similar decrease in thermal diffusivity with time over the inter-ELM interval was inferred for the ions in the steep-gradient region around $\rho \approx 0.96$ for shot 119436, but not for shot 98889, in which the decrease in thermal diffusivity was inferred inside of the edge pedestal. It should be noted that the time resolution for the T_i measurements was 10 ms for shot 98889.

Acknowledgement

Work partially supported by DOE Grant DE-FG02-00-ER54538 with the Georgia Tech Research Corporation for collaboration as a member of the DIII-D National Tokamak Facility Team.

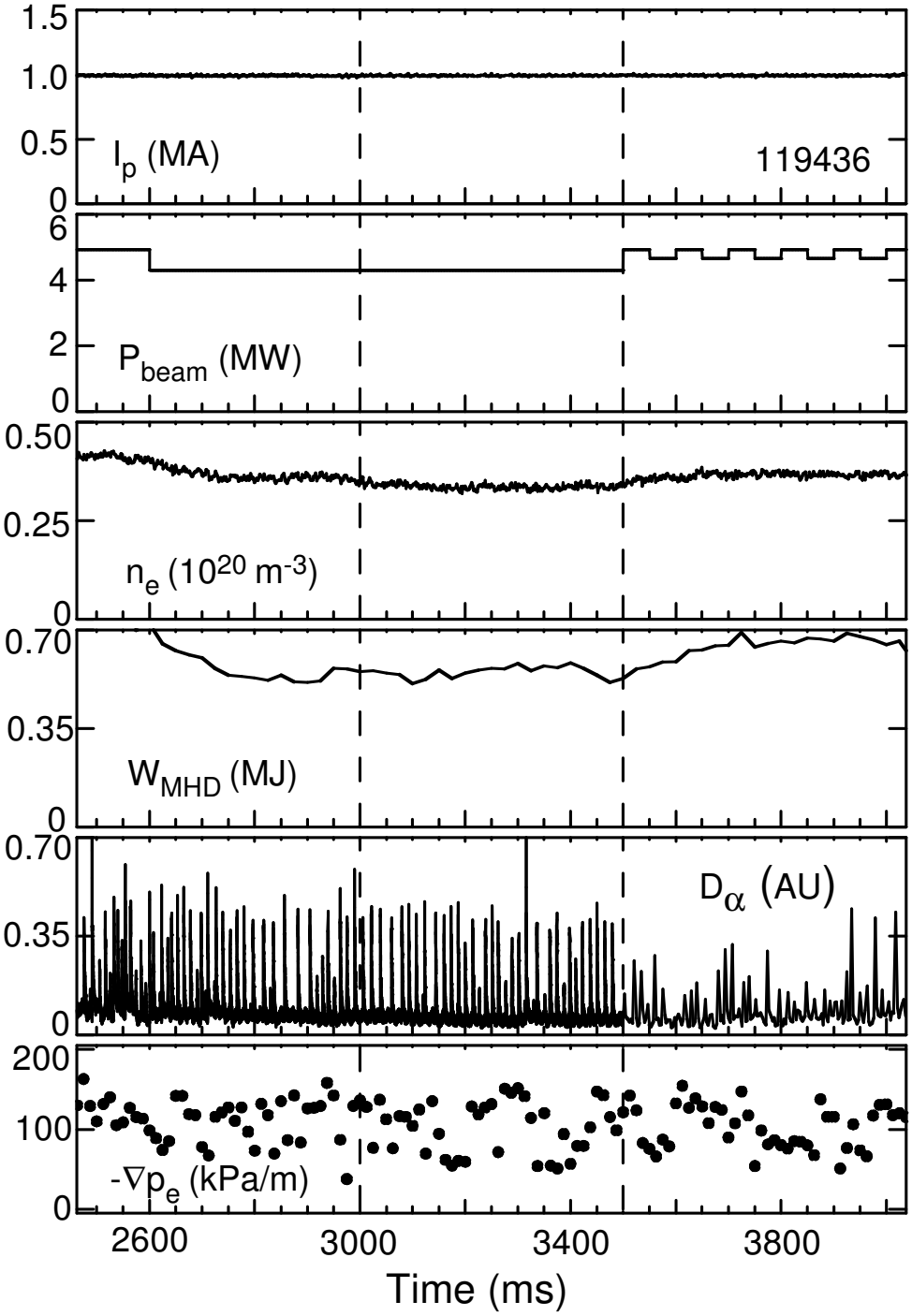

Fig. 1 Data traces for DIII-D shot 119436 (I_p=plasma current, P_{beam}= neutral beam power, n_e=line average global density, W_{MHD}=global plasma energy, D_α=Lyman alpha signal, ∇p_e pedestal pressure gradient)

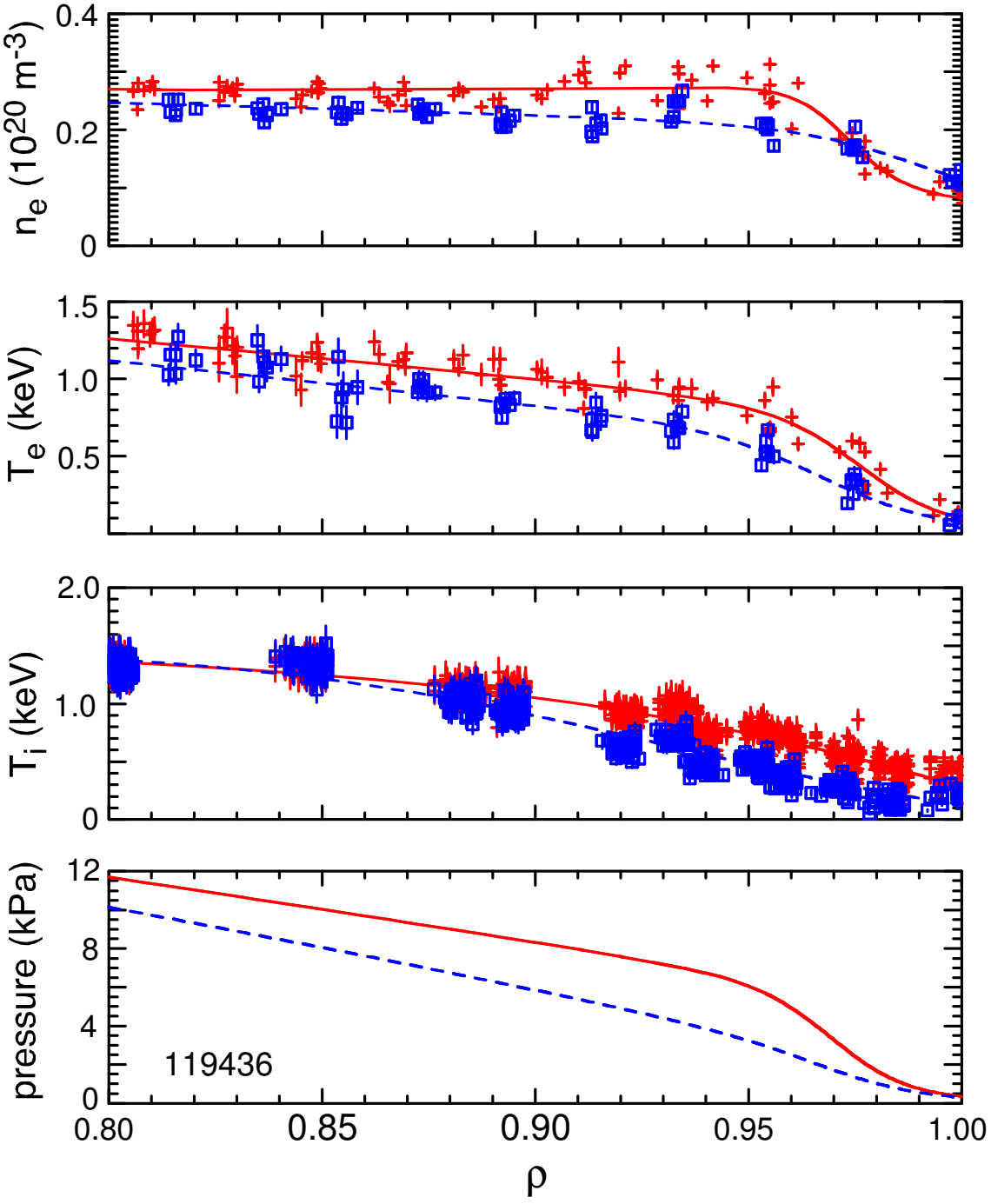

Fig. 2 Density, temperatures and pressure in edge region of DIII-D shot 119436 (squares=data 10-20% after ELM crash, +=data 80-99% after ELM crashes, dashed line=fit 10-20% after ELM crash, solid line=fit 80-99% after ELM crashes) ρ= normalized radius.

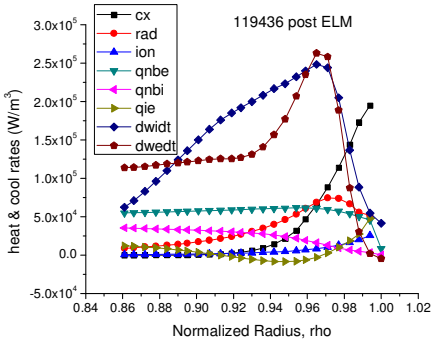

Fig. 3a Heating and cooling rates 10-20 % after ELM crash in 119436.

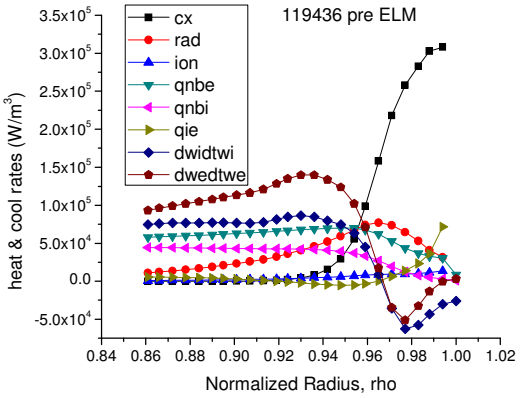

Fig. 3b Heating and cooling rates 80-99% after ELM crash in 119436.

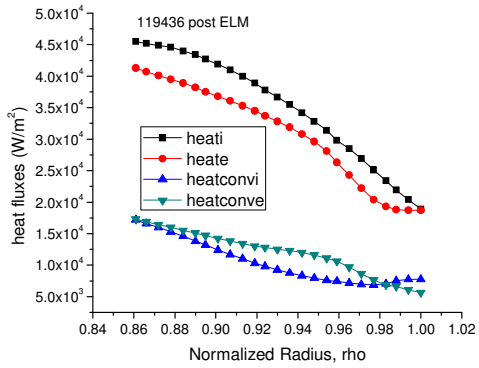

Fig. 4a Radial heat fluxes (total and convective) for ions and electrons at 10-20 % after ELM crash in 119436.

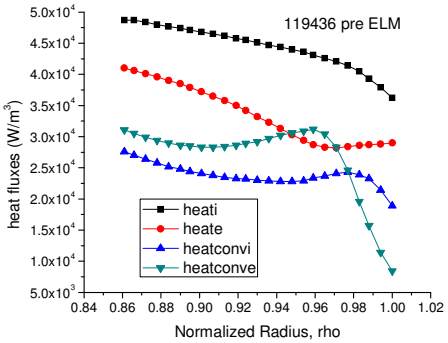

Fig. 4b Radial heat fluxes (total and convective) for ions and electrons at 80-99 % after ELM crash

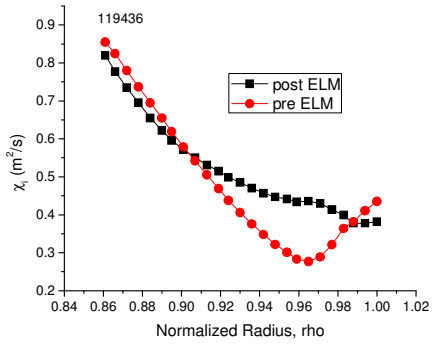

Fig. 5a Inferred exp. χ_i 10-20% and 80-99 % after ELM crash in 119436.

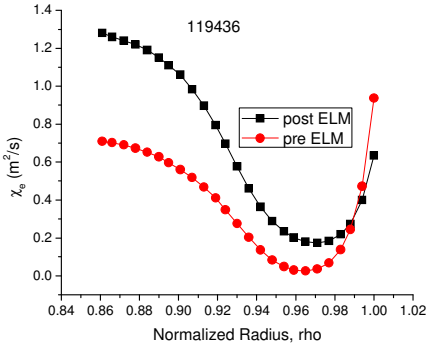

Fig. 5b Inferred exp. χ_e 10-20 % and 80-99 % after ELM crash in 119436.

References

1. R. J. Groebner and T. H. Osborne, Phys. Plasmas, 5, 1800 (1998).
2. A. E. Hubbard, R. L. Boivin, R. S. Granetz, et al., Phys. Plasmas, 5, 1744 (1998).
3. W. Suttrop, O. Gruber, B. Kurzan, et al., Plasma Phys. Controlled Fusion, 42, A97 (2000).
4. T. H. Osborne, J. R. Ferron, R. J. Groebner, et al., Plasma Phys. Controlled Fusion, 42, A175 (2000).
5. M. Kotschenreuther, W. Dorland, Q. P. Liu, et al., Proceedings of the 16th Conference on Plasma Physics Controlled Fusion Research, Montreal, 1996 (IAEA, Vienna, 1997), Vol. 2, p 371.
6. J. E. Kinsey, R. E. Waltz and D. P. Schissel, Proceedings of the 24th European Physical Society, Berchtesgarten, 1997, Vol. III, p 1081. Plasma Phys. Controlled Fusion, 42, A97 (2000).
7. G. D. Porter, R. Isler, J. Boedo and T. D. Rognlien, Phys. Plasmas, 7, 3663 (2000).
8. D. P. Coster, X. Bonnin, K. Borrass, et al., Proceedings of the 18th Fusion Energy Conference, Sorrento, Italy, 2000 (IAEA, Vienna, 2001).
9. W. M. Stacey and R. J. Groebner, Phys. Plasmas, 13, 072510 (2006).
10. W. M. Stacey and R. J. Groebner, Phys. Plasmas, 14, 012501 (2007).
11. W. M. Stacey and T. E. Evans, Phys. Plasmas, 13,112506 (2006).
12. P. Gohil, M. A. Mahdavi, L. Lao, *et al*., Phys. Rev. Lett., 61, 1603 (1988).
13. A. W. Leonard, J. A. Boedo, M. E. Fenstermacher, *et al.*, J. Nucl. Mater., 313-316, 768 (2003).
14. A. Loarte, G. Saibene, R. Sartori, *et al*., Phys. Plasmas, 11, 2668 (2004).
15. I. Zeng, G. Wang, E. J. Doyle, *et al.*, Plasma Phys. Control. Fusion, 46, A121 (2004).
16. I. Nunes, M. Manso, F. Serra, *et al.*, Nucl. Fusion, 45, 1550 (2005).
17. M. R. Wade, K. H. Burrell, J. T. Hogan, *et al.* , Phys. Plasmas, 12, 056120 (2005).
18. M. Yoshida, S. Kobayashi, H. Urano, *et al.*, Plasma Phys. Control. Fusion, 48, A209 (2006).
19. T. N. Carlson, G. L. Campbell, J. C. DeBoo, et al., Rev. Sci. Instrum., 63, 4901 (1992).

20. P. Gohil, K. H. Burrell, R. J. Groebner, et al., *Proceedings of the 14th Symposium on Fusion Engineering, San Diego, 1991* (Inst. Electrical & Electronics Engineers, New York, 1992), Vol. 2, p. 1199.
21. W. Pfeiffer, F. B. Marcus, C. J. Armentrout, *et al.*, Nucl. Fusion, 25, 655 (1985).
22. W. M. Stacey, E. W. Thomas and T. M. Evans, Phys. Plasmas, 2, 3740 (1995); 4, 678 (1997).
23. R. Hulse, Nucl. Technol. Fusion, 3, 259 (1983).
24. W. M. Stacey, Phys. Plasmas, 5, 1015 (1998); 8, 3673 (2001); Nucl. Fusion, 40, 678 (2000).
25. P. Gohil, K. H. Burrell, R. J. Groebner, et al., *Proceedings of the 14th Symposium on Fusion Engineering, San Diego, 1991* (Inst. Electrical & Electronics Engineers, New York, 1992), Vol. 2, p. 1199.
26. W. Pfeiffer, F. B. Marcus, C. J. Armentrout, *et al.*, Nucl. Fusion, 25, 655 (1985).
27. W. M. Stacey, E. W. Thomas and T. M. Evans, Phys. Plasmas, 2, 3740 (1995); 4, 678 (1997).
28. R. Hulse, Nucl. Technol. Fusion, 3, 259 (1983).
29. W. M. Stacey, Phys. Plasmas, 5, 1015 (1998); 8, 3673 (2001); Nucl. Fusion, 40, 678 (2000).

C. INTEGRATED CORE-PEDESTAL-DIVERTOR-NEUTRALS MODELING

W. M. Stacey, Georgia Tech

Abstract

A self-consistent solution of the core particle and power balances, of the 1D particle, momentum and energy balances in the scrape-off layer and divertor, and of the 2D transport of the recycling and fueling neutrals back into the divertor and the core plasma constitutes the basic integrated modeling calculation. Subsidiary calculations are then made to evaluate the onset of density limiting thermal instabilities and the L-H power threshold, and to calculate the pedestal structure, the inferred experimental thermal diffusivities and momentum transport rates in the edge pedestal, and the rotation and E_r profiles in the edge. Available experimental data is used in the calculation.

Introduction

A simple, but comprehensive, integrated core-divertor-neutrals code [1] for analyzing and interpreting edge plasma data in DIII-D has been under development for DIII-D analysis for several years. The basic integrated modeling code, the supplementary calculations of the onset conditions for various density-limiting thermal instabilities, and the calculation of the structure and transport in the edge pedestal are summarized.

Calculation of Plasma and Neutrals Distributions

Coupled Core-Divertor-Neutrals Calculation

The GTIM code iteratively solves three coupled modules, depicted in Fig. 1. Equations are given in [1].

1) The Core module solves the core particle and power balance equations for the core temperature and density and the particle and power fluxes into the SOL. Input to the particle balance includes the NBI particle source; from experiment the "die-away" particle confinement time, the pedestal and line-average densities, the density radial profile factors; and the recycling and fueling neutral source calculated by the Neutrals module. Experimental input to the power balance calculation includes the ohmic and auxiliary heating powers, the core radiative power, the energy confinement time, the impurity density, the pedestal temperature and temperature profile factors.

2) The Divert module solves the density, momentum and energy balance equations, with sheath boundary conditions, integrated over the scrape-off layer and divertor from the stagnation point to the divertor plate (the "2-point" model). This yields the density and temperature at the stagnation point and at the divertor plate and the ion flux incident on the divertor plate, which is recycled as a neutral atom source for the Neutral module. Radiative, ionization and elastic scattering/charge exchange cooling rates, elastic scattering/charge exchange momentum dissipation, and the ionization particle source and recombination particle sink are included in the calculation, using neutral atom densities calculated by the Neutrals module. The particle and heat fluxes into the SOL from the core calculated by the Core module are also input for the Divert calculation.
3) The Neutrals module calculates the recycling of ions from the divertor plate and of charge-exchange neutrals from the plasma and divertor chamber walls via reflection (as atoms) and re-emission (as molecules which are immediately dissociated) and the transport of these atoms through the divertor and SOL and private flux regions into the core. This module also calculates the transport into the core of neutral gas puffed into the plasma chamber. The experimental plasma densities and temperatures at the core separatrix and pedestal, and the plasma densities in the divertor and SOL calculated by the Divert module, are used for the neutral penetration calculation. The recycling source from the walls is adjusted so that the line-averaged density calculated by the core module matches the experimental value.

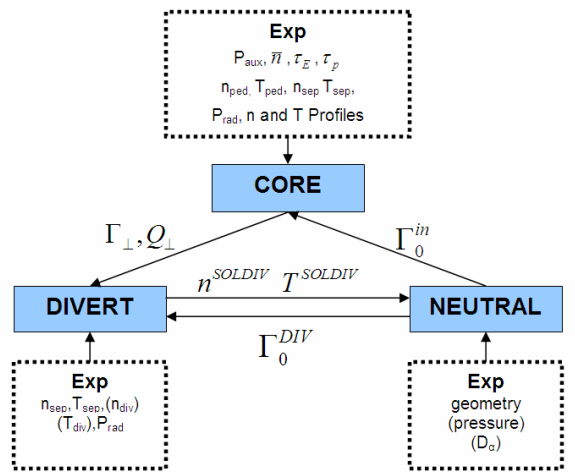

Fig. 1 Schematic of GTIM Calculation

Neutrals Module

The neutral transport model is based on an extension of the Interface Current Balance integral transport method known as the TEP method (section 16.6 of [2]). A simplified geometric model of the DIII-D divertor, private flux, plenum, scrape-off layer and plasma edge [3,4] is 'hardwired' into the present Neutrals module, with input for the variable separatrix strike point, X-point and other geometric locations taken from experiment (EFIT). This module will soon be replaced by the GTNEUT code [5].

Particle sources are treated as follows. The ion flux incident on the divertor target plates (calculated by the Divert module) and the charge-exchange neutral flux incident on the chamber and divertor walls (calculated by the Neutrals module) are recycled as atoms or re-emitted as molecules (section 13.2 of [2]), with probabilities which depend on the surface material and the incident particle energy. The molecules immediately dissociate into lower energy atoms that are transported as such until their first collision, after which they take on the same energy distribution as the other atoms at that location. The gas puff fueling is treated as a molecular source which immediately dissociates into lower energy atoms. The experimental plasma densities measured by Thomson scattering at the separatrix and at the pedestal near the core mid-plane are used in the neutral attenuation calculation.

Divert Module

The Divert model [4] is an extended "2-point" model in which the 1D particle, momentum and energy balance equations in the scrape-off layer and divertor are integrated from the stagnation point to the divertor plate, and stagnation and sheath (section 13.1 of [2]) boundary conditions are used. The model includes calculated impurity radiation and atomic physics cooling, momentum dissipation due to charge-exchange and elastic scattering, ion particle sources due to ionization of neutrals and ion particle sinks due to recombination. The input particle and heat fluxes from the core into the SOL and the recycling neutral influx into (primarily) the divertor plasma are the primary sources to the Divert model. The plasma density and temperature are calculated at the stagnation point and at the divertor plate, and interpolated in between.

Prediction of Density-Limiting Thermal Instabilities

Detachment

An analysis of the 2-point equations with sheath boundary conditions [6,7] indicates that there is an upper limit on the separatrix density at the stagnation point for which a solution can be obtained. Although this limit is properly associated with detachment (i.e. the sheath boundary conditions are no longer correct), it was shown to predict the disruption density limit in ASDEX relatively well and used as a surrogate for a disruption density limit. However, other devices (e.g. DIII-D) operate with partial detachment at the separatrix. This limiting density for detachment (which is not strictly speaking a thermal instability) can be found numerically as the largest stagnation density at which the integrated modeling code GTIM can obtain a solution.

Disruption

"Density-limit" disruptions are preceded by radial collapse of the temperature profile, hence of the current channel, so that the onset of radiative collapse of the temperature profile serves as a surrogate for onset of a "density limit" drisruption. A linear stability analysis of the radial particle and power balance equations in the core plasma with respect to perturbations with the form of a radiative collapse of the temperature profile leads to an expression for the maximum average plasma density for which the plasma is thermally stable against temperature collapse [8]. This disruption density limit is evaluated using experimental ion and impurity densities and temperature and using the calculated edge neutral density.

MARFE

Multifaceted asymmetric radiation from the edge (MARFE) is observed to occur in most tokamaks above a certain limiting density. Linear stability analysis of the 2D particle, momentum and energy balance equations in the plasma edge (inside the separatrix) with respect to 2D perturbations in the poloidal distributions of density, temperature and flow leads to an expression for the threshold edge density for the onset of MARFEs [9]. This expression is evaluated using measured plasma density and temperature (and their radial gradients) and impurity concentrations in the edge, and using calculated neutral densities. For analysis of DIII-D, in which the MARFE first forms at the X-point, the neutral density calculated in the X-point edge region, which is much larger than the average neutral density in the edge, is used to evaluate the limiting edge plasma density for MARFE onset.

Divertor MARFE

As the density increases sufficiently in diverted tokamaks, the plasma partially detaches from the target plate and a dense, cool radiating region forms near the divertor target. With further increase in density, a sudden redistribution occurs in which the dense radiating region shifts upstream to the vicinity of the X-point, but remains outside the separatrix. This phenomenon is referred to as a "divertor MARFE" (although the radiative condensation mechanism involved in MARFEs that occur on closed field lines inside the separatrix is not present).

A linear stability analysis of the of the 1D particle, momentum and energy balance equations in the SOL and divertor with respect to perturbations along the field lines with wave lengths comparable to the distance along the field lines from the divertor plate to the X-point leads to a rather complicated dispersion relation which is evaluated numerically for the growth rate of the perturbation [10]. A positive grow rate indicates a prediction of a divertor MARFE. The multiple growth rates (roots of the dispersion relation) are evaluated numerically using the density and temperature in the SOL and divertor calculated by the Divert module.

Edge transport enhancement

A linear analysis of the particle, momentum and energy balance equations for ions and electrons in the edge region (inside the separatrix) with respect to 2D (radial-perpendicular) perturbations with short radial wave lengths (comparable to the transport barrier width) in the density, velocity and temperature distributions indicates that such perturbations may be driven

unstable by impurity radiation and ionization and charge-exchange cooling phenomena [11]. The enhanced radial transport associated with such unstable perturbations is $\Delta\chi \approx \omega\lambda^2$. The linear growth rates $\omega_{i,e}$ for such instabilities in the ion and electron balance equations in the edge are evaluated using measured plasma density and temperatures (and their radial gradients), measured impurity concentrations, and calculated neutral concentrations in the plasma edge inside the separatrix.

L-H and H-L transition threshold

Combining the prediction (discussed in the previous paragraph) of linear growth rates of short radial wavelength thermal instabilities with the requirement for removing a given radial heat flux through the edge leads to a coupling of edge temperature gradients and transport coefficients and the prediction of a threshold value of the edge power flux above which the edge transport coefficients rapidly decrease because of stabilization of the thermal instability and edge temperature gradients sharply increase; i.e. an edge transport barrier forms [12]. This power flux can be associated with the threshold power for the L-H transition [13]; it is evaluated using the measured plasma density and temperature and impurity concentration in the edge, the calculated neutral density in the edge, and the calculated ion particle flux through the edge.

Edge Pedestal Modeling

Edge pedestal pressure and density structure

Momentum balance requirements constrain the ion pressure gradient to satisfy $L_{pi}^{-1} = \left(\upsilon_{ri} - \upsilon_{pi}\right)\big/\widehat{D}_i$, where υ_{ri} is the radial ion flux determined by solution of the continuity equation and υ_{pi} is a pinch velocity that must be evaluated from momentum inputs and rotation velocities [14]. The quantity $-\partial n_i / n_i \partial r = L_{pi}^{-1} - L_{Ti}^{-1}$, the continuity equation, and the neutral influx equation of the Neutrals module (for the ionization source) are solved iteratively for the ion and neutral atom distributions in the edge, using the experimental values of n_i^{sep} at the separatrix, L_{Ti}^{-1} and the rotation velocities and radial electric field (to evaluate υ_{pi}). Calculated density profiles agree with directly measured density profiles in the edge of several DIII-D shots [15].

Inference of experimental thermal diffusivities in the plasma edge

Solving the heat balance equations for ions and electrons and the continuity equation (both with experimental separatrix boundary conditions) and the neutral influx equations of the Neutrals module simultaneously allows determination of the conductive heat flux profiles, which can be used together with the measured temperature profiles in the edge to infer ion and electron thermal diffusivities [16]. Calculation of the neutral density profiles enables radiation and atomic physics cooling to be taken into account, and calculation of the nv_r distribution allows convective effects to be taken into account. This methodology can be used to interpret differences in transport in different operating regimes (a representative example is shown in Fig. 2), and to compare various theoretical predictions of thermal diffusivities, using measure edge temperature and density profiles [17,18].

Momentum transport, rotation velocity and radial electric field profiles

An inference of the experimental rate of radial transport of toroidal angular momenturm is calculated from the toroidal angular momentum equation, using the measured carbon v_ϕ [19].

A calculation [20] of the poloidal and toroidal rotation velocities and the radial electric field in the plasma edge has been implemented, but is not yet fully operational.

Acknowledgement

Work partially supported by DOE Grant DE-FG02-00-ER54538 with the Georgia Tech Research Corporation for collaboration as a member of the DIII-D National Tokamak Facility Team.

References

1. W. M. Stacey, Contrib. Plasma Phys., 42, 199 (2002); Phys. Plasmas, 5, 1015 (1998); Phys. Plasmas, 8, 3673 (2001); Nucl. Fusion, 40, 965 (2000).
2. W. M. Stacey, *Fusion Plasma Physics*, Wiley-VCH, Weinheim (2005).
3. W. M. Stacey, Nucl. Fusion, 40, 965 (2000).
4. W. M. Stacey, Phys. Plasmas, 5, 1015 (1998).
5. J. Mandrekas, Comput. Phys. Commun., 161, 36 (2004).
6. K. Borrass, Nucl. Fusion, 31, 1035 (1991).
7. K. Borrass, R. Schneider and R. Farengo, Nucl. Fusion, 37, 523 (1997).
8. W. M. Stacey, Phys. Plasmas, 4, 1069 (1997).
9. W. M. Stacey, Plasma Phys. Control. Fusion, 39, 1245 (1997); Fusion Technol., 36, 38 (1999).

10. W. M. Stacey, Phys. Plasmas, 8, 525 (2001).
11. W. M. Stacey, Phys. Plasmas, 6, 2452 (1999).
12. W. M. Stacey et al., Phys. Plasmas, 9, 3082 (2002).
13. W. M. Stacey, Phys. Plasmas, 10, 3949 (2003); 11, 686 (2004); 12, 072518 (2005).
14. W. M. Stacey, 11, 1511 (2004); 11, 4295 (2004); 13, 012513 (2006).
15. W. M. Stacey and R. J. Groebner, Phys. Plasmas, 12, 042504 (2005).
16. W. M. Stacey and R. J. Groebner, Phys. Plasmas, 13, 072510 (2006).
17. W. M. Stacey and T. E. Evans, Phys. Plasmas, 13, 112506 (2006).
18. W. M. Stacey and R. J. Groebner, Phys. Plasmas, 14, 012501 (2007).
19. W. M. Stacey and R. J. Groebner, Phys. Plasmas, 13, 012513 (2006).
20. W. M. Stacey, Contrib. Plasma Phys., 46, 597 (2006).

D. ION PARTICLE TRANSPORT IN THE EDGE PEDESTAL

W. M. Stacey, Georgia Tech

Abstract

A generalized pinch-diffusion transport relation previously derived from momentum conservation is combined with the continuity equation to derive a "generalized diffusion theory" for ion particle transport in the tokamak plasma edge inside the separatrix. The resulting generalized diffusion coefficients are evaluated for a representative experiment.

Introduction

We have previously derived [1,2] a generalized pinch-diffusion relation in the plasma edge region from momentum and particle balance. This pinch-diffusion relation was used to explain the steep pressure gradients in the edge of high confinement (H-mode) plasmas in terms of the requirements of momentum and particle conservation in the presence of recycling neutrals. The requirements of momentum and particle balance were manifest in the radial electric field and rotation velocity profiles acting through the pinch velocity term. While the implications of these previous results for particle transport in the plasma edge are implicit, they have not heretofore been explicitly set forth, which is thus the purpose of this work.

Particle and Momentum Balance

The time-independent particle continuity equation for ion species 'j' is

$$\nabla \cdot \Gamma_j \equiv \nabla \cdot n_j \boldsymbol{\upsilon}_j = S_j \tag{1}$$

where $S_j(r,\theta) = n_e(r,\theta) n_{j0}(r,\theta) \langle \sigma\upsilon \rangle_{ion} \equiv n_e(r,\theta) \nu_{ion}(r,\theta)$ is the ionization source rate of ion species 'j' and n_{j0} is the local concentration of neutrals of species 'j'. The time-independent momentum balance equation for ion species "j" is

$$\nabla \bullet \left(n_j m_j \boldsymbol{\upsilon}_j \boldsymbol{\upsilon}_j \right) + \nabla p_j + \nabla \cdot \boldsymbol{\pi}_j = n_j e_j \left(\boldsymbol{\upsilon}_j \times \boldsymbol{B} \right) + n_j e_j \boldsymbol{E} + \boldsymbol{F}_j + \boldsymbol{M}_j - n_j m_j \nu^j_{elcxj} \boldsymbol{\upsilon}_j \tag{2}$$

where $\mathbf{E}$ represents the electric field, $\mathbf{F}_j$ represents the interspecies collisional friction, $\mathbf{M}_j$ represents the external momentum input rate, and the last term represent the momentum loss rate due to elastic scattering and charge exchange with neutrals of all ion species 'k'[$\nu_{atj} = \Sigma_k n^c_{k0} (\langle \sigma\upsilon \rangle_{el} + \langle \sigma\upsilon \rangle_{cx})_{jk}$].

The FSA radial component of Eq. (2) may be written to leading order as

$$E_r^0 = \frac{1}{n_j^0 e_j}\frac{\partial p_j^0}{\partial r} + \upsilon_{\phi j}^0 B_\theta^0 - \upsilon_{\theta j}^0 B_\phi^0 \tag{3}$$

Torque Representations

In order to evaluate the FSA (flux surface average) toroidal component of Eq. (2) it is necessary to evaluate the FSA toroidal viscous torque and inertial terms in that equation. The neoclassical viscous torque can be written as the sum of "parallel", "gyroviscous", and "perpendicular" components [3,4]. Since the flux surface average of the "parallel" component of the toroidal viscous torque vanishes identically, the flux surface averaged toroidal viscous torque may be written as the sum of the "gyroviscous" and "perpendicular" components

$$\left\langle R^2 \nabla\phi \bullet \nabla \bullet \Pi \right\rangle = \left\langle R^2 \nabla\phi \bullet \nabla \bullet \Pi \right\rangle_{gv} + \left\langle R^2 \nabla\phi \bullet \nabla \bullet \Pi \right\rangle_{\perp} \tag{4}$$

where

$$\left\langle R^2 \nabla\phi \bullet \nabla \bullet \Pi \right\rangle_{gv} = -\left\langle \frac{1}{Rh_p}\frac{\partial}{\partial l_\psi}\left(R^3 h_p \eta_4 \frac{\partial}{\partial l_p}\left(\upsilon_\phi / R\right)\right)\right\rangle \tag{5}$$

and

$$\left\langle R^2 \nabla\phi \bullet \nabla \bullet \Pi \right\rangle_{\perp} = -\left\langle \frac{1}{Rh_p}\frac{\partial}{\partial l_\psi}\left(R^3 h_p \eta_2 \frac{\partial}{\partial l_\psi}\left(\upsilon_\phi / R\right)\right)\right\rangle \tag{6}$$

in a right-hand (ψ, p, ϕ) toroidal flux surface coordinate system, where $\eta_2 = nT\tau/(\Omega\tau)^2$ and $\eta_4 \approx (\Omega\tau)\eta_2 \approx (10^3\text{-}10^4)\eta_2$, where $\Omega \equiv ZeB/m$ and τ is the collision frequency, so that the "gyroviscous" toroidal torque is generally a couple of orders of magnitude larger than the "perpendicular" toroidal viscous torque. Approximating the flux surface geometry by toroidal geometery and making a low order Fourier expansion $X(r,\theta) = X^0(r)\left[1 + X^c \cos\theta + X^s \sin\theta\right]$ for the densities and rotation velocities allows Eqs. (3) and (4) to be written in a form exhibiting an explicit momentum transfer frequency

$$\left\langle R^2\nabla\phi\bullet\nabla\bullet\Pi\right\rangle_{gvj} \approx \frac{1}{2}\eta_{4j}\frac{r}{R_0}\left(L_n^{-1}+L_T^{-1}+L_{\upsilon_\phi}^{-1}\right)\left[\left(4+\tilde{n}_j^c\right)\tilde{\upsilon}_{\phi j}^s+\tilde{n}_j^s\left(1-\tilde{\upsilon}_{\phi j}^c\right)\right]\upsilon_{\phi j}\equiv R_0 n_j^0 m_j \nu_{gvj}\upsilon_{\phi j} \quad (7)$$

and

$$\left\langle R^2\nabla\phi\bullet\nabla\bullet\Pi\right\rangle_{\perp j} \approx R_0\eta_{2j}\left[L_{\upsilon_\phi}^{-1}\left(\frac{1}{r}-L_{\eta_2}^{-1}\right)-\frac{1}{\upsilon_{\phi j}}\frac{\partial^2\upsilon_{\phi j}}{\partial^2 r}\right]\upsilon_{\phi j}\equiv R_0 n_j^0 m_j \nu_{\perp j}\upsilon_{\phi j} \qquad (8)$$

where the poloidal asymmetry coefficients $\tilde{n}_j^c \equiv n_j^c/\varepsilon$, etc. can be determined by solving the low order Fourier moments of the poloidal component of the momentum balance [4].

Turbulent, or "anomalous", toroidal viscous torque is usually assumed to be of the form of Eq. (6) with an enhanced viscosity coefficient η_{anom}, leading to

$$\left\langle R^2\nabla\phi\bullet\nabla\bullet\Pi\right\rangle_{anomj} \approx R_0\eta_{anomj}\left[L_{\upsilon_\phi}^{-1}\left(\frac{1}{r}-L_{\eta_2}^{-1}\right)-\frac{1}{\upsilon_{\phi j}}\frac{\partial^2\upsilon_{\phi j}}{\partial^2 r}\right]\upsilon_{\phi j}\equiv R_0 n_j^0 m_j \nu_{anomj}\upsilon_{\phi j} \qquad (9)$$

Equation (1) can be used to write the inertial term in the FSA toroidal component of Eq. (2) as

$$\left\langle R^2\nabla\phi\bullet\nabla\bullet\left(n_j m_j \mathbf{\upsilon}_j\mathbf{\upsilon}_j\right)\right\rangle = \left\langle R^2\nabla\phi\bullet n_j m_j\left(\mathbf{\upsilon}_j\bullet\nabla\right)\mathbf{\upsilon}_j\right\rangle + R_0 n_j m_j \nu_{ionj}\upsilon_{\phi j} \qquad (10)$$

and the same set of approximations can be used to write the first term on the right as

$$\begin{aligned}\left\langle R^2\nabla\phi\cdot n_j m_j\left(\upsilon_j\bullet\nabla\right)\upsilon_j\right\rangle \simeq \frac{1}{2}\Big(&\frac{\upsilon_{rj}}{R_o}\left\{\varepsilon\left(1+\tilde{n}_j^c+\tilde{\upsilon}_{\phi j}^c\right)-2R_o L_{\upsilon_\phi j}^{-1}\right\}-\\ \varepsilon\frac{\upsilon_{\theta j}^0}{R_o}&\left\{\tilde{\upsilon}_{\phi j}^s\left(1+\tilde{n}_j^c+\tilde{\upsilon}_{\theta j}^c\right)-\tilde{\upsilon}_{\theta j}^s\left(1+\tilde{\upsilon}_{\phi j}^c\right)-\tilde{\upsilon}_{\phi j}^c\tilde{n}_j^s\right\}\Big)n_j m_j R_0\upsilon_{\phi j}^0 \equiv R_0 n_j m_j \nu_{nj}\upsilon_{\phi j}^0\end{aligned} \qquad (11)$$

Pinch-Diffusion Transport Relation

The above results may be used to write the FSA toroidal component of Eq. (2) as

$$n_j^0 m_j \nu_{jk}^0\left(\left(1+\beta_j\right)\upsilon_{\phi j}^0-\upsilon_{\phi k}^0\right) = n_j^0 e_j E_\phi^A + e_j B_\theta^0\Gamma_{rj} + M_{\phi j}^0, \qquad (12)$$

where

$$\beta_j \equiv \frac{\nu_{gvj}^0+\nu_{\perp j}^0+\nu_{anomj}^0+\nu_{nj}^0+\nu_{elcxj}^0+\nu_{ionj}}{\nu_{jk}^0} \equiv \frac{\nu_{dj}^*}{\nu_{jk}^0} \qquad (13)$$

Now, combining the radial and toroidal components of the FSA momentum balance equations—Eqs. (3) and (12)--yields a generalized pinch-diffusion relation [7] for the radial particle flux

$$\Gamma_{rj} \equiv \left\langle n_j \upsilon_{rj} \right\rangle = n_j D_{jj} \left(L_{nj}^{-1} + L_{Tj}^{-1} \right) - n_j D_{jk} \left(L_{nk}^{-1} + L_{Tk}^{-1} \right) + n_j \upsilon_{pj} \tag{14}$$

where the "diffusion coefficients" are given by

$$D_{jj} \equiv \frac{m_j T_j \left(\nu_{dj}^* + \nu_{jk} \right)}{\left(e_j B_\theta \right)^2} \quad , \quad D_{jk} \equiv \frac{m_j T_k \nu_{jk}}{e_j e_k (B_\theta)^2} \tag{15}$$

and the pinch velocity is given by

$$n_j \upsilon_{pj} \equiv -\frac{M_{\phi j}}{e_j B_\theta} - \frac{n_j E_\phi^A}{B_\theta} + \frac{n_j m_j \nu_{dj}^*}{e_j B_\theta} \left(\frac{E_r}{B_\theta} \right) + \frac{n_j m_j f_p^{-1}}{e_j B_\theta} \left(\left(\nu_{jk} + \nu_{dj}^* \right) \upsilon_{\theta j} - \nu_{jk} \upsilon_{\theta k} \right) \tag{16}$$

A sum over the '*k*' terms is understood when more than two ion species are present. The quantity $f_p^{-1} \equiv B_\phi / B_\theta$.

Subject to the assumption that there in a single impurity species (I) distributed with the same radial distribution and the same local temperature as the main ions (i), Eq. (14) can be written as a constraint on the main ion pressure gradient [1,2]

$$L_{pi}^{-1} \equiv -\frac{1}{p_i} \frac{dp_i}{dr} = \frac{\upsilon_{ri} - \upsilon_{pinch,i}}{D_i} \tag{17}$$

and momentum balance can be used to reduce Eq. (16) to

$$\upsilon_{p,i} = \frac{\left[-M_{\phi i} - n_i e_i E_\phi^A + n_i m_i \left(\nu_{iI} + \nu_{di}^* \right) \left(f_p^{-1} \upsilon_{\theta i} + E_r / B_\theta \right) - n_i m_i \nu_{iI} \upsilon_{\theta I} \right]}{n_i e_i B_\theta} \tag{18}$$

where the effective main ion diffusion coefficient in this approximation is

$$D_i = \frac{m_i T_i \nu_{iI}}{\left(e_i B_\theta \right)^2} \left[1 + \frac{\nu_{di}^*}{\nu_{iI}} - \frac{Z_i}{Z_I} \right] \tag{19}$$

We have previously found [1,2] that when the pinch velocity of Eq. (18) was evaluated from experiment, the radial particle flux was determined by solving the continuity Eq. (1) in the presence of recycling neutrals, and L_{Ti} was taken from experiment, that

$$\frac{-1}{n_i} \frac{\partial n_i}{\partial r} \equiv L_{ni}^{-1} = L_{pi}^{-1} - = \frac{\upsilon_{ri} - \upsilon_{p,i}}{D_i} - L_{Ti}^{-1} \tag{20}$$

could be integrated inward from an experimental separatrix boundary condition to obtain a density profile with a pedestal structure that was in good agreement with the edge density profile obtained from Thomson scattering (when corrected for the presence of impurities). The pinch velocity term, determined primarily by the measured rotation velocity and radial electric field profiles, was found to be the dominant factor in determining the density profile.

Generalized Radial Diffusion Theory

Since diffusion theory is generally used to describe ion particle transport in plasma edge codes [5,6], it is of interest to compare the radial transport theory implied by the above relations with the form of diffusion theory commonly used in the plasma edge codes. Using the generalized pinch-diffusion relation of Eq. (16) in the continuity Eq. (1), which governs Γ_{rj}, yields the coupled set of generalized diffusion equations that determine the particle distribution in the edge plasma for ion species "*j*", $\nabla \cdot \mathbf{\Gamma}_j = S_j$, the radial component of which can be written for each species in the slab limit appropriate in the plasma edge

$$-\frac{\partial}{\partial r}\left(D_{jj}\frac{\partial n_j}{\partial r}\right)-\frac{\partial}{\partial r}\left(D_{jk}\frac{\partial n_k}{\partial r}\right)-\frac{\partial}{\partial r}\left(D_{jj}\frac{n_j}{T_j}\frac{\partial T_j}{\partial r}\right)- \frac{\partial}{\partial r}\left(D_{jk}\frac{n_j}{T_k}\frac{\partial T_k}{\partial r}\right)+\frac{\partial\left(n_j \upsilon_{pj}\right)}{\partial r}= S_j \qquad (21)$$

Again, the "*jk*" subscript indicates a sum over "*k*". Note that the 'self-diffusion' coefficient D_{jj} involves all the momentum transport rates for species "j" (i.e. atomic physics, viscous, anomalous, etc. as well as the interspecies collisional momentum exchange frequency for species "j"). There is an Eq. (21) for each ion species in the plasma, and they are coupled.

The generalized diffusion theory of Eq. (21), which was rigorously derived from momentum balance and the continuity equation for each ion species in the plasma, is different in several respects from the usual ad hoc form of diffusion theory [Eq. (21) but retaining only the first term on the left side] that is commonly used to represent radial particle transport in plasma edge fluid codes. First, the diffusion equation for species "j" depends not only on the density gradient of species "j", but on the density gradients for all other ion species as well. Second, the diffusion equation for species "j" depends on the temperature gradients for all ion species. This

implies that, when used in the predictive mode, the diffusion equations for all the ion densities and the heat balance equations for all the ion temperatures are coupled and must be solved simultaneously.

The second major difference is that there is a convection term with a pinch velocity [Eq.(16)] that depends on the poloidal rotation velocities for all the ion species and on the radial electric field, the induced toroidal electric field, and the neutral beam (or any other) external momentum input or torque. As discussed above, we have previously found [1,2] that the pinch velocity was the dominant term in the pinch-diffusion relation insofar as the determination of the edge density profile. Thus, we anticipate that the convective last term on the left in Eq. (21) will have a major effect on the calculation of the ion particle profile in the edge plasma. This implies that when Eq. (21) is used in the predictive mode, the rotation equations must also be solved simultaneously with the particle and heat diffusion equations. Solution of the rotation equations in the plasma edge has been discussed elsewhere [7], but remains to be carried out simultaneously with the particle and energy transport equations.

Diffusion Coefficients and Pinch Velocities

The profiles of v_d^* (inferred from experiment [2]), v_{iI} and v_{Ii} ($n_I m_I v_{Ii} = n_i m_i v_{iI}$ by momentum conservation) were used (together with the experimental temperature profile) to calculate the profiles of the diffusion coefficients defined by Eqs. (15) for a DIII-D H-mode shot, as shown in Fig. 1. The sharp increase in the experimentally inferred v_d^* just inside the separatrix results in a sharp increase in the "self-diffusion" coefficients D_{ii} and D_{II} just inside the separatrix. Because the main ion self-diffusion coefficient $D_{ii} >> D_{iI}$, the first and third terms in Eq. (21), involving the main ion density and temperature gradients, are much more important than the second and fourth terms involving the impurity ion density and temperature gradients, in the main ion diffusion equation. On the other hand, since the impurity self-diffusion coefficient $D_{II} << D_{Ii}$, the second and fourth terms involving the main ion density and temperature gradients are much more important in the impurity ion equation than are the terms involving the impurity ion density and temperature gradients.

The contributions of the various components of the deuterium pinch velocity given by Eq. (18) are shown in Fig. 2 for a DIII-D H-mode shot. The normalized radius is in terms of poloidal flux. The inward pinch velocity is quite large in the edge.

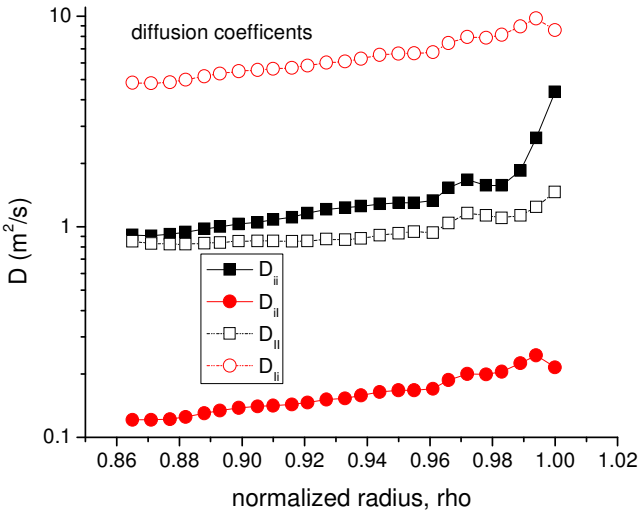

Fig. 1: Generalized diffusion coefficients in the edge of DIII-D H-mode shot 92976

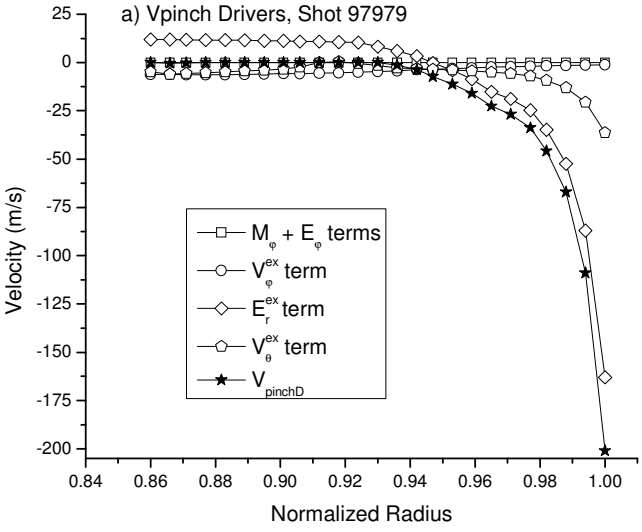

Fig. 2 Pinch velocity in the edge of DIII-D H-mode shot 97979

Summary and Conclusions

The requirements of conservation of ion momentum and particle density lead directly to a generalized diffusion equation for each ion species, with diffusion-like terms involving the gradients of all ion densities and temperatures and a convective term involving a "pinch velocity" consisting of rotation velocities, the radial electric field and other terms. The definitions of the pinch velocity and of the diffusion coefficients follow directly from the derivation from momentum balance.

These equations are quite different than the diffusion equations normally used to analyze the radial transport of particles in tokamak edge transport codes (e.g. [5] and [6]). For example, in these references the radial particle transport was modeled using only the first diffusion term on the left in Eq. (21) and neglecting the pinch term. The value of the "self-diffusion" coefficient was inferred from experiment by adjusting it to force the calculation (with three of the diffusion terms and the pinch term of Eq. (21) set to zero) to 'match' the experimental density profile. It is clear from Figs. 1 and 2 that this type of diffusion approximation and fitting procedure neglects a lot of physics.

References

1. W. M. Stacey, Phys. Plasmas, 11, 4295 (2004).
2. W. M. Stacey and R. J. Groebner, Phys. Plasmas, 13, 012513 (2006).
3. W. M. Stacey and D. J. Sigmar, Phys. Fluids, 28, 2800 (1985).
4. W. M. Stacey, R. W. Johnson and J. Mandrekas, Phys. Plasmas, 13, 062508 (2006).
5. L. D. Horton, A. V. Chankin, Y. P. Chen, *et al*., Nucl. Fusion, 45, 856 (2005).
6. G. D. Porter, R. Isler, J. Boedo and T. D. Rognlien, Phys. Plasmas, 7, 3663 (2000).
7. W. M. Stacey, Contrib. Plasma Phys., 46, 597 (2006).

E. NEUTRAL TRANSPORT ANALYSIS OF DIII-D EXPERIMENTS

W. M. Stacey and Z. W. Friis, Georgia Tech
L. Lao and R. J. Groebner, General Atomics

Abstract

An effort is underway to make the fast 2D neutral atom transport code GTNEUT available for routine experimental analysis of DIII-D experiments.

Introduction

It is becoming increasingly clear that the interaction of recycling and gas fueled neutral atoms with the plasma in the divertor and plasma edge have a significant impact on many plasma phenomena (MARFE formation, pedestal structure, L-H transition, etc.) However, the generally available capability to analyze neutral transport in tokamak experiments is either overly simplified (assumption that a certain fraction of the ions exiting the plasma are reflected as neutrals atoms and a 1D calculation of their penetration into the plasma) or impractically computationally intensive (Monte Carlo).

A novel adaptation of neutron transport methodology has been developed at Georgia Tech for neutral atom transport calculations in the geometrically complex edge and divertor regions. This transmission-escape probability (TEP) method[1] has been benchmarked against Monte Carlo in a series of model problems designed to test approximations[2,3] and in the analysis of DIII-D experiments[4-6], and refinements to the basic methodology have been developed[6]. The TEP methodology has been implemented in two codes: i) as a geometrically simplified model of the DIII-D divertor and SOL (see Ref. 4) in the NEUTRAL subroutines in the GTIM integrated modeling code described in section D; and ii) as an arbitrarily complex geometrical model in the GTNEUT code[7]. The GTNEUT code has been found in calculations of DIII-D to achieve accuracy comparable to Monte Carlo at orders of magnitude smaller cpu times[6], making it a good candidate for routine analysis of neutral fueling and recycling in DIII-D experiments.

The primary challenge to implementing the GTNEUT code for routine experimental analysis for DIII-D is providing the 2D distribution of plasma density in the divertor, scrape-off layer and edge plasma inside the separatrix that is needed to provide the “background” plasma properties for the neutal transport calculation. This problem has been dealt with for the

NEUTRAL subroutines in the GTIM code by a combination of i) using Thomson data for the electron temperature and density and CERS data for the ion density in the plasma edge and scrapeoff layer near the core midplane, ii) calculating the plasma density and temperature on the separatrix in front of the divertor strike point using a "2-point" divertor model, iii) physics-based extrapolation (e.g. exponential radial attenuation of density and temperature in the SOL according to Bohm transport and observed flux expansion in the divertor), and iv) normalization to match other experimental observations (e.g. line averaged core plasma density, energy confinement time). This procedure has been shown[4] to yield a calculated neutral distribution in reasonably good agreement with Monte Carlo calculations and with DIII-D measurements. However, the geometric model for the neutral calculation in GTIM is "hardwired" for a particular divertor configuration and does not provide the detail nor the geometric flexibility of the geometry model in GTNEUT.

Coupling of the GTNEUT and GTIM Codes

PhD thesis research by Z. W. Friis has begun to investigate the effects of neutral atoms on various edge phenomena observed in DIII-D and TEXTOR. The computational basis for this thesis will be a combination of the GTNEUT and GTIM codes, augmented by experimental input. Although this development is in an early stage, the general intent is to use the GTIM code and experimental data, as at present, to provide the "background" plasma parameters for GTNEUT, then to run GTNEUT to provide a more detailed neutral distribution (and perhaps to iterate this procedure). We are presently interacting with DIII-D staff with regard to additional experimental input that can be used to augment this determination of a "background" plasma for GTNEUT. Once this coupled GTIM-GTNEUT calculation is made, then the GTIM subroutines that calculate MARFE onset, pedestal structure, inferred edge thermal diffusivities, etc. will be used to investigate the effect of neutral atoms on these phenomena, and other models will be developed and evaluated for other phenomena. An effort will be made to automate this calculation procedure (to whatever degree feasible) and make it available to other interested members of the DIII-D Team.

Coupling of the ONETWO and GTNEUT Codes

There is interest within the DIII-D Team in coupling the GTNEUT code to the 1.5D core transport code ONETWO[8]. Two challenges have been identified: i) providing the "background" plasma properties for GTNEUT; and ii) providing a geometric region structure for GTNEUT that is compatible with ONETWO and with the source of background plasma properties. The GTNEUT—GTIM package discussed above, augmented by ONETWO results within the separatrix, has been identified as a likely possibility for dealing with the "background" plasma properties issue. (A plasma edge fluid code such as UEDGE or B2.5, with GTNEUT as the neutral calculation, is another possibility for the longer term.)

The coupling of ONETWO and the GTNEUT—GTIM package is conceptually straightforward. ONETWO would provide particle and heat fluxes from the core across the separatrix into the SOL to the divertor plasma model in GTIM. The divertor plasma model in GTIM would calculate the ion flux incident on the divertor plate which would be input to GTNEUT. GTNEUT would calculate the recycling neutral flux at the divertor plate and the recycling charge-exchange neutral flux at the walls and would transport these recycling sources plus any gas puffing sources through the divertor and SOL regions across the separatrix into the core to provide a poloidally dependent neutral fueling source for ONETWO.

References

1. W. M. Stacey and J. Mandrekas, Nucl. Fusion, 34, 1385 (1994).
2. R. Rubilar, W. M. Stacey and J. Mandrekas, Nucl. Fusion, 41, 1003 (2001).
3. W. M. Stacey, J. Mandrekas and R. Rubilar, Fusion Sci. Technol., 40, 66 (2001).
4. W. M. Stacey, Nucl. Fusion, 40, 965 (2000).
5. J. Mandrekas, R. J. Colchin, W. M. Stacey, et al., Nucl. Fusion, 43, 314 (2003).
6. D.-K. Zhang, J. Mandrekas and W. M. Stacey, Phys. Plasmas, 13, 062509 (2006).
7. J. Mandrekas, Comp. Phys. Comm., 161, 36 (2004).
8. W. Pfeiffer, F. B. Marcus, C. J. Armentrout, *et al.*, Nucl. Fusion, 25, 655 (1985).

F. SUB-CRITICAL TRANSMUTATION REACTORS WITH TOKAMAK FUSION NEUTRON SOURCES BASED ON ITER PHYSICS AND TECHNOLOGY

W. M. Stacey, Georgia Tech

Abstract

A series of design scoping and fuel cycle studies for sub-critical fast transmutation reactors driven by tokamak fusion neutron sources has been carried out to determine if the requirements on the tokamak neutron sources are compatible with the fusion physics and technology design database that will exist after the operation of ITER and to determine if there is a significant advantage in fuel cycle flexibility due to sub-critical operation that would justify the additional cost and complexity of a fusion neutron source. The fast reactor technologies are based on reactor concepts being developed in the DoE Generation-IV and Advanced Fuel Cycle initiatives.

Introduction

For many years there has been a substantial international R&D activity devoted to closing the nuclear fuel cycle. During the 1990s this activity emphasized the technical evaluation of transmutation reactors that would fission the transuranic (TRU) content of the accumulating spent nuclear fuel (SNF) discharged from conventional nuclear power reactors[1-4], thus reducing the requirements for long-term geological high-level waste repositories (HLWRs) for the storage of SNF. With the recently increasing recognition that nuclear power is the only environmentally sustainable way to meet the world's expanding energy requirements in the near term, the emphasis in the new century has broadened to also include extracting more of the potential energy content in uranium by first transmuting the "fertile" ^{238}U into fissionable ^{239}Pu. This growing realization of the need for an expanded global role for nuclear power has led to a number of government policy inititatives aimed at closing the nuclear fuel cycle—the Advanced Fuel Cycle Initiative (AFCI), the Generation-IV Initiative (GEN-IV) and most recently the Global Nuclear Energy Partnership (GNEP).

There would be advantages in being able to operate the transmutation reactors sub-critical, with a neutron source to provide the neutrons needed to maintain the fission chain reaction, e.g.

the achievement of higher levels of burnup for a given batch of TRU fuel. Almost all of the studies in the 1990s of sub-critical transmutation reactors were based on use a proton accelerator with a spallation target as a neutron source, although there were a few studies of the use of D-T fusion neutron sources.

The concept of using a D-T tokamak fusion neutron source based on ITER physics and technology[5] to drive a sub-critical fast transmutation reactor based on nuclear and separations technologies being evaluated in the AFCI[6] and GEN-IV[7] initiatives has been developed in a series of studies[8-19] at Georgia Tech over the past several years. The general design objective was a 3000 MWth, passively safe, sub-critical fast reactor driven by a fusion neutron source that could fission the TRU in the SNF discharged annually by three 1000 MWe LWRs. The general fuel cycle objective was > 90% burnup of this TRU (in order to reduce the HLWR requirements by an order of magnitude relative to the present once-through LWR fuel cycle) while minimizing the nuclear fuel reprocessing steps. The designs were constrained to use ITER physics and technology for the fusion neutron source, to use nuclear and reprocessing technology being evaluated in the GEN-IV and AFCI studies, to use extensions of existing nuclear fuel technology but with TRU, and to achieve tritium self-sufficiency for the fusion neutron source.

The FTWR and GCFR Studies

Sub-critical transmutation reactors based on two of the nuclear technologies being developed in the GEN-IV studies have been examined in the Georgia Tech studies. The Fusion Transmutation of Waste Reactor (FTWR) series of studies was based on a variant of the Lead Cooled Fast Reactor and the Sodium Cooled Fast Reactor in the GEN-IV initiative--a fast-spectrum reactor using a metal fuel consisting of TRU alloyed with zirconium in a zirconium matrix and cooled by a liquid metal (Li17Pb83 eutectic), which also served as the tritium breeder. The Gas Cooled Fast Transmutation Reactor (GCFTR) series of studies was based on a variant of the Gas Cooled Fast Reactor in the GEN-IV initiative--a fast-spectrum reactor using TRU-oxide fuel in coated TRISO particle form in a SiC matrix cooled by He. Both the FTWR and GCFTR cores are annular and located outboard of the toroidal plasma chamber. The core plus plasma chamber were surrounded first by a reflector (tritium breeding blanket for GCFTR)

and then by a shield to protect the magnets from radiation damage and heating, as indicated in Fig. 1 for the GCFTR design.

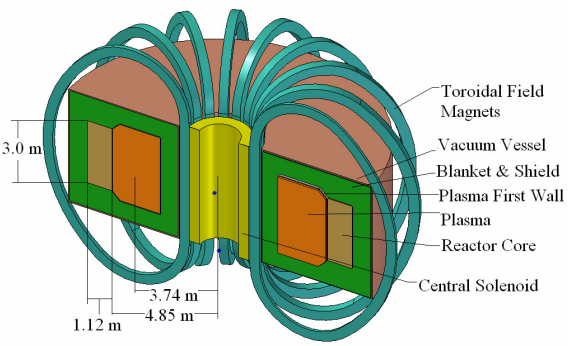

Fig. 1 Gas Cooled Fast Transmutation Reactor

The ANL metal fuel, liquid metal cooled reactor design[20] was adapted to accommodate Pb-Li eutectic coolant and TRU-Zr fuel for the FTWR designs. The fast, He-cooled reactor designs being developed under the GEN-IV Program guided the choice of the GCFTR core design, and the coated fuel particle technology being developed in the NGNP program[21] was adapted for TRU-oxide fuel for the GCFTR. Tritium breeding was accomplished in the Pb-Li coolant in the FTWR designs and in a Li_2O blanket surrounding the plasma and reactor core in the GCFTR designs.

The fusion technology was based on the ITER design[5,22]. The superconducting magnet design was based directly on the ITER cable-in-conduit design scaled down to maintain the same stress level. The first-wall and divertor designs were adapted from the ITER design to accommodate the different coolants. A LHR heating and current drive system was adapted from ITER.

The radial build dimensions of the FTWR and GCFTR concepts were determined from the engineering and physics constraints[22] and are given in Table I.

Tokamak Neutron Source

The principal tokamak neutron source parameters for the FTWR and GCFTR series of transmutation reactors are given in Table II. The requirements on β_N and confinement are within

the range routinely achieved in present experiments, and the requirements on β_N, confinement, energy amplification Q_p, and fusion power level are at or below the ITER level, except for the FTWR-AT and GCFTR-3 design concepts. The requirement on the current-drive efficiency, after calculation of bootstrap current fraction using ITER scaling, is only somewhat beyond what has been achieved to date (γ_{CD} = 0.45 in JET and 0.35 in JT60-U). The ongoing worldwide tokamak program is addressing the current-drive/bootstrap current/steady-state physics issue. The current-drive efficiency/bootstrap fraction needed for FTWR/GCFTR is certainly within the range envisioned for Advanced Tokamak operation and may be achieved in ITER. Although single numbers are given for the parameters in Table II, there is a range of operating parameters within which a given neutron source intensity (fusion power level) can be achieved, as shown in Fig. 2 for a 7.2MA design that can achieve P_{fus} = 200 MW.

TABLE I Dimensions (m) of FTWR and GCFTR Designs

Parameter	**FTWR**	**FTWR-SC**	**FTWR-A**	**GCFTR**	**GCFTR-2**	**GCFTR-3**
Major Radius, R_0	3.10	4.50	3.86	4.15	3.74	3.76
Fluxcore, R_{fc}	1.24	1.10	0.65	0.66	0.66	0.88
CS+TF, Δ_{mag}	0.57	1.68	1.20	1.50	1.13	0.91
Refl+Shld, Δ_{rs}	0.40	0.65	0.90	0.86	0.87	0.89
Plasma, a_{plasma}	0.89	0.90	1.10	1.04	1.08	1.08
Core						
Inner Radius, R_{in}	4.00	5.40	5.00	5.25	4.84	4.85
Radial Width, W	0.40	0.40	0.40	1.12	1.12	1.12
Height, H	2.28	2.28	2.28	3.00	3.00	3.00

Transmutation Reactor Cores

FTWR

The fuel is a transuranic zirconium alloy (TRU-10Zr) dispersed in a zirconium matrix in pin form and clad with a ferritic steel similar to HT-9. The relative amounts of transuranics and zirconium in the fuel region are adjusted to achieve the desired neutron multiplication (k_{eff} = 0.95) at the beginning of each burn cycle. At equilibrium, the transuranics will constitute approximately 45% of the fuel volume. The annular transmutation reactor core is outboard of the plasma, and both are surrounded by reflector and shield (Fig. 1). The design of the FTWR

transmutation reactor is based on the ANL ATW reactor design studies[20]. The same pin and assembly geometry was used, with the exception that the length of the assembly was increased to 228 cm. Table III gives the basic data for the fuel assembly design. The reactor core is 40 cm thick and consists of 470 assemblies, 1/5 of which will be 'half assemblies' placed in the gaps along the interior and exterior surfaces of the reactor region to produce a more uniform annular distribution.

For 3000 MW_{th} total reactor power uniformly distributed in the fuel pins, the volumetric heat source is q''' = 42.2 MW/m^3. The main coolant parameters are given in Table III. The required pumping power is 130 MW, the majority of which is needed to overcome MHD losses.

TABLE II Tokamak Neutron Source Parameters for FTWR and GCFTR Transmutation Reactors[a]

Parameter	**FTWR[9]**	**FTWR -SC[10]**	**FTWR -AT[11]**	**GCFTR[12]**	**GCFTR -2[13]**	**GCFTR -3[14]**	**ITER[5]**
Max. Fusion power, P_{fus} (MW)	150	225	500	180	180	500	410
Max.Neutron source, $S_{fus}(10^{19}$ #/s)	5.3	8.0	17.6	7.1	7.1	17.6	14.4
Major radius, R (m)	3.1	4.5	3.9	4.2	3.7	3.7	6.2
Aspect ratio, A	3.5	5.0	3.5	4.0	3.4	3.4	3.1
Elongation, κ	1.7	1.8	1.7	1.7	1.7	1.7	1.8
Current, I (MA)	7.0	6.0	8.0	7.2	8.3	10.0	15.0
Magnetic field, B (T)	6.1	7.5	5.7	6.3	5.7	5.9	5.3
Safety factor, q_{95}	3.0	3.1	3.0	3.0	3.0	4.0	
Confinement, $H_{IPB98}(y,2)$	1.1	1.0	1.5	1.0	1.0	1.06	1.0
Max. Normalized beta, β_N	2.5	2.5	4.0	2.0	2.0	2.85	1.8
Max. Plasma Power Mult., Q_p	2.0	2.0	4.0	2.9	3.1	5.1	10
CD efficiency,γ_{cd} (10^{-20} A/Wm^2)	0.37	0.23	0.04	0.5	0.61	0.58	
Bootstrap current fraction, f_{bs}	0.40	0.50	≥0.90	0.35	0.31	0.26	
Max. Neut. Flux, Γ_n (MW/m^2)	0.8	0.8	1.7	0.9	0.6	1.8	0.5
Max. FW Heat flux, q_{fw} MW/m^2)	0.34	0.29	0.5	0.23	0.23	0.65	0.15

Availability (%)	≥ 50	≥ 50	≥ 50	≥ 50	≥ 50	≥50	

[a] Calculated on the basis of the physics and engineering constraints described in Ref. 22. All superconducting except FTWR. All based on ITER physics except AT.

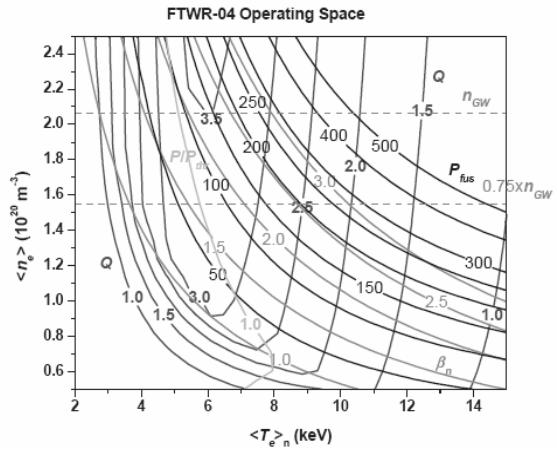

Fig. 2 Operating Space for 7.2 MA Neutron Source that Achieves up to P =$_{fus}$ 200 MW

GCFTR

Design concepts were developed for several TRISO (tri-material isotropic) and BISO (bi-material isotropic) particles. The reference TRISO particle (Fig. 3) has a TRU-oxide kernel (330 μm diameter) surrounded by a 50% porous buffer layer (73 μm) of ZrC to allow for fission product recoil and gas buildup. Next is an inner WC layer (10 μm), then a SiC structural layer (67 μm), and finally an outer WC layer (15 μm). These particles are embedded in a SiC matrix, then formed into a fuel pin clad with ODS steel, as indicated in Table III. Nominal thermal parameters are given in Table III. A He coolant v/o ≥ 25% would be adequate for heat removal under normal operating conditions.

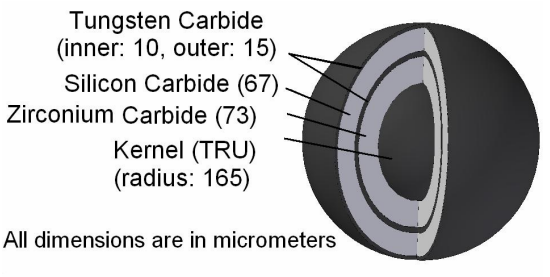

Fig. 3 TRISO Fuel Particle

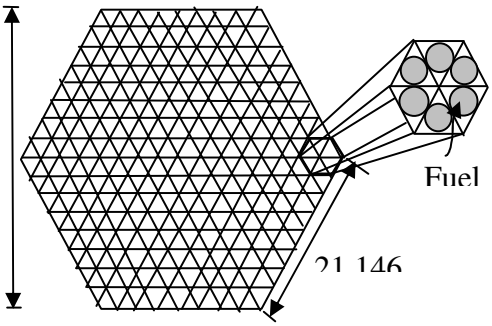

Fig. 4 Fuel Assembly for GCFTR

A cross-section of the fuel assembly for the GCFTR is shown in Fig. 4, and the materials composition for the two reactor types are given in Table IV.

TABLE III Core and Fuel Assembly Parameters

		FTWR	**GCFTR**
Core in radius, cm		500	485
Core width, cm		40	112
Core height, cm		228	300
Pin Diameter, cm		0.635	1.526
Pins per assembly		217	384
Assy. Flat to Flat,cm		16.1	36.6
Assy. Length, cm		228	300
Assemblies in Core		470	245
Core Cool Flow,kg/s		51630	3280
Coolant T_{in}/T_{out} , ^{o}K		548/848	553/767
Materials (v/o)	Fuel	20	60
	Structure	10	10
	Coolant	70	30

TABLE IV Materials Compositon of FTWR and GCFTR

Component	**FTWR**	**GCFTR**
Reactor		
Fuel	TRU-Zr metal in Zr matrix	TRU-oxide TRISO,SiC matrix
Clad/structure	FeS/FeS	ODS/ODS
Coolant	LiPb	He
Trit. Breeder	LiPb	Li_2O

Reflector	FeS, LiPb	ODS, He, Li_2O
Shield	FeS, LiPb, B_4C, ZrD_2, W	ODS, HfC, Ir, Cd, WC, B_4C, He
Magnets	NbSn,NbTi/He (OFHC/LN_2)	NbSn/He
First-Wall	Be-coated FeS, LiPb	Be-coated ODS, He
Divertor	W-tiles on Cu-CuCrZr, LiPb	W-tiles on Cu – CuCrZr, He

A direct Brayton cycle would be used to convert the 3000 MWt to 1020 MWe. Taking into account power requirements to run the GCFTR, the net electrical power produced would be ≈ 700 MWe.

Fuel Cycle Analysis

The great advantage of sub-critical operation is the variety of transmutation fuel cycles that it makes available, some of which are examined in this section. The composition changes in the fuel cycle were calculated with the REBUS fuel cycle code[23] and the ORIGEN-S burnup code[24].

FTWR

In the FTWR reference fuel cycle[15] the fuel will remain in the reactor for 5 burn cycles of 564 days each and then be reprocessed, blended with 'fresh' SNF and fabricated into new fuel elements for re-insertion into a FTWR. The fuel will be "shuffled" to a new location in the reactor after each burn cycle and removed for reprocessing after the fifth burn cycle.

A first generation FTWR operating at 3000 MWt will process approximately 74 MT of transuranics from LWR SNF, of which approximately 56% will be fissioned, 0.2% will be lost to the waste streams, and 44% will be recycled in a second generation FTWR. The second and subsequent generations of FTWRs will use the fuel from the previous generation FTWRs and therefore operate in the equilibrium mode shown in Table V over their entire life. BOC and EOC refer to beginning and end of cycle.

TABLE V: An Equilibrium 5-Batch Reprocessing Fuel Cycle for 3000 MWt TRU Fueled FTWR (23 MT Initial TRU Load)[15]

Burn cycle, d	564

5-batch residence, y	7.7
TRU burn/residence, %	29
SNF disposed, MT/yr	101
Fast fluence/residence, 10^{23} n/cm^2	3.4
BOC k_{eff}	0.925
EOC k_{eff}	0.836
BOC P_{fus}, MW	61
EOC P_{fus}, MW	150

Repeated recycling of the discharged transuranics from FTWRs in successive generations of FTWRs will ultimately result in the destruction of up to 99.4% of the transuranics discharged from LWRs. At equilibrium, each 3000 MWt FTWR would be able to process the TRU discharged from three 3000 MWt conventional LWRs, so that it is possible to envision a fleet of conventional and transmutation reactors in the thermal power ratio 3/1.

GCFTR

A similar reprocessing fuel cycle was developed for the GCFTR, as indicated in Table VI. However, the emphasis in the GCFTR studies was achieving > 90% burnup of the TRU in the coated fuel particles *without reprocessing* and then removing the > 90% depleted fuel from the reactor and directly depositing it in a HLW repository. Leaving the highly depleted fuel, together with the accumulated fission products in the reactor long enough to achieve such deep burnup would lead to a much less reactive core (e.g. lower multiplication factor, k). The results in Table VI are indicative of the burnup (about 15%) that can be achieved without reprocessing and with $P_{fus} \leq$ 200 MW.

TABLE VI: An Equilibrium 5-Batch Re-processing Fuel Cycle for 3000 MWt TRU Fueled GCFTR (37 MT Initial TRU Load)[17]

Burn cycle, d	376
5-batch residence, y	5.2
TRU burn/residence, %	15.3
SNF disposed, MT/yr	98
Fast fluence/residence, 10^{22} n/cm^2	3.9
BOC k_{eff}	0.936
EOC k_{eff}	0.900
BOC P_{fus}, MW	122
EOC P_{fus}, MW	199

By increasing the limit on the fusion neutron source from 200-500 MW [$P_{fis} \sim k_{eff} P_{fus} / (1 - k_{eff})$][25],

it is possible to extend the allowable reactivity decrement due to burnup and accumulation of fission products, hence to increase the length of the burn cycle. Several 5-batch, "once-through", non-reprocessing fuel cycles in which the reactivity decrement associated with fuel burnup was compensated by an increase in neutron source strength to obtain a longer burn cycle length are summarized in Table VII. A 400 MW fusion neutron source enables achievement of a 5-batch, 2400 day burn cycle, fuel cycle in a 3000 MWt GCFTR, which is sufficient to obtain > 90 % TRU burnup without reprocessing.

TABLE VII: Once-Through Steady-State 5-Batch Non-Reprocessing Fuel Cycles for 3000 MWt TRU Fueled GCFTR (37 MT Initial TRU Load)[14]

Burn cycle, d	600	1200	1800	2400
5-batch residence, y	8.2	16.4	24.7	32.9
TRU burnup, %	24.9	49.7	72.4	93.7
SNF disposed, MT/yr	101	101	98	95
Fast Fluence, 10^{23} n/cm^2	0.7	1.3	3.0	4.3
BOC k_{eff}	0.987	0.917	0.856	0.671
EOC k_{eff}	0.927	0.815	0.714	0.611
BOC P_{fus}, MW	13	83	144	329
EOC P_{fus}, MW	73	185	286	389

More efficient utilization of the energy content of uranium not only requires that the TRU in SNF discharged from conventional LWR reactors be recovered and fissioned, but that some significant fraction of the > 99% of natural uranium that is ^{238}U be transmuted to ^{239}Pu and subsequently fissioned. Two possible steady state fuel cycles for a GCFTR fueled with a mixture of 70% ^{238}U and 30% TRU in oxide form are shown in Table VIII. A 3000 MWt GCFTR with a 500 MWt fusion neutron source could achieve > 75% utilization of the energy content of uranium (as compared to the present < 1%).

TABLE VIII: Once-Through Steady-State 5-Batch Non-Reprocessing Fuel Cycles for 3000 MWt 30%TRU-70% ^{238}U Fueled GCFTR (37 MT Initial TRU + ^{238}U Load)[14]

Parameter		
Burn cycle, d	600	1800
5-batch residence, y	8.2	24.7
TRU+ ^{238}U burnup, %	24.9	72.4
Fast fluence, 10^{23} n/cm^2	1.2	4.4
BOC k_{eff}	0.590	0.577
EOC k_{eff}	0.576	0.534
BOC P_{fus}, MW	410	423
EOC P_{fus}, MW	424	466

Tritium Self-Sufficiency

Tritium accumulation calculations were performed in order to insure that the amount of tritium produced during operation is enough for the plasma to be self-sufficient. In the FTWR the Li-PB coolant was also the tritium breeder. For GCFTR, a tritium breeding blanket about 15 cm thick surrounded the plasma chamber and reactor core. Lithium oxide (Li_2O) was chosen as a representative form for the lithium, although hydroxide formation problems may require another form (e.g. lithium silicate or titinate). On-line extraction of tritium from Li_2O requires operation between 400 ºC and 800 ºC. Below 400 ºC the rate of tritium diffusion out of the individual grains of Li_2O is too slow, and above 800 ºC the particles swell and seal off porous channels through which the tritium must percolate to reach the helium purging channels.

The total mass of lithium in the GCFTR blanket is 2.24×10^5 kg, and the total volume of the lithium blanket is 7.07×10^7 cm^3. Calculations used the flux distributions from a multigroup r-z model in the ORIGEN-S burnup code to calculate the producion and decay of the tritium in the blanket.

The amount of tritium that must be produced over a burn cycle for self-sufficiency is the amount required to replace the tritium burned over that burn cycle and to provide for one week of operation after restart, allowing for a 60-day decay between shutdown and restart of the next cycle. For the 600 day burn cycle, this requirement is for the production of 63.8 kg over the cycle. The calculations described above predict the production of 64.1 kg over the cycle, from which it may be concluded that the GCFTR-3 is tritium self-sufficient.

Component Lifetimes

The design lifetime of the FTWR and GCFTR neutron source is 40 years at 75% availability, or 30 EFPY. The superconducting magnets are shielded to reduce the fast neutron fluence to the superconductor and the rad dose to the insulators below their respective limits—10^{19} n/cm^2 fast neutron fluence for Nb_3Sn and 10^9 rads for organic insulators (10^{12} rads for ceramic insulators). The first-wall of the plasma chamber and the plasma-facing part of the divertor will accumulate fast neutron fluences of 7.5 and 5.8x10^{23} n/cm^2, respectively, over the 30 EFPY lifetime. The radiation damage limit of the ferritic or ODS steel first-wall structure is estimated to be 1.5-3.0x10^{23} n/cm^2, which implies that it will be necessary to replace the first-wall 2-4 times over the 30 EFPY lifetime. Erosion of the divertor by the incident plasma ion flux will necessitate several replacements over the 30 EFPY lifetime.

The achievement of the fuel cycles discussed above of course is contingent on the reactor fuel and structure radiation damage lifetimes. The FTWR fuel cycle would accumulate a fast neutron fluence of 3.4x10^{23} n/cm^2 over a 5-batch residence time, which is at the upper limit of the estimated lifetime fluence for the ferritic steel cladding and assembly structure. The fuel would then be reprocessed, reclad , recycled and placed into a new structural assembly. The similar reprocessing fuel cycle for the GCFTR would accumulate a fast neutron fluence of 3.9x10^{22} n/cm^2 over a 5.2 year residence time, while the non-reprocessing GCFTR fuel cycles of Table IX would accumulate up to 4.3x10^{23} n/cm^2. Unfortunately, there is little data for TRISO particles in fast spectra.

Component radiation damage lifetime estimates are summarized in Table IX.

TABLE IX. Component Radiation Damage Lifetimes

Component	**GCFTR-3 fast neutron fluence n/cm^2>0.1MeV)**	**LIMIT fast neutron fluence (n/cm^2>0.1MeV)**
Reactor		
Clad		
8.2 yr, 25% TRU burnup	6.9x10^{22}	1.5-3.0x10^{23} [a] ?
32.9yr, 94% TRUburnup	4.3x10^{23}	1.5-3.0x10^{23} [a] ?
TRISO Fuel particle		
8.2 yr, 25%	6.9x10^{22}	?

TRU burnup		
32.9yr, 94% TRUburnup	$4.3x10^{23}$	?
Neutron Source		
TFC Nb_3Sn 30 EFPY	$1.6x10^{18}$	$1x10^{19}$ [b]
TFC insul 30EFPY	$3.1x10^{7}$ rad	10^{9}-10^{12} rad [b]
First-wall 30EFPY	$7.5x10^{23}$	1.5-3.0$x10^{23}$ [a] ?
Divertor		Plasma erosion

[a] estimated 100-200 dpa [b] M. Sawan U. Wisc.

Passive Safety

A thermal analysis of the core was performed under severe LOCA (loss-of-coolant) conditions--complete loss of normal core cooling. It was assumed that the neutron source was immediately shut down and that all heat addition came from decay heat, which was calculated using the ORIGEN-S code at a burnup of 3000 days with a fuel composition of 30% U-238/ 70% TRU. The initial decay heat represented 8.8% of total thermal output, falling to 2.4% after one hour.

Once coolant is lost, the only significant process for removing heat is through thermal radiation transfer. The results of a sophisticated computation[26] of a LOCA in the annular core of a helium cooled Prismatic Fueled Reactor (PFR) were scaled according to surface area and temperature to obtain values for the amount of heat rejected from the core by radiation in the GCFTR-3. Using the mass, specific heat, and scaled rejection heat of the reactor core, the temperature change of the clad was calculated, as shown in Fig.5. The clad inner temperature peaks at 2736K well above the melting point of the clad material (1600K) and the fuel (2300K).

An accumulator system was designed to provide emergency core cooling. The accumulator design was a ring header in the shape of a torus, which was located beneath the core. Attached to the torus were 24 55m^3 standby helium tanks. The torus is connected to the reactor via four 6 inch inner diameter injection headers, each containing a flow restrictor and check valve in series,

and the entire system was pressurized to 6 MPa. The effectiveness of the accumulator is shown in Fig. 5.

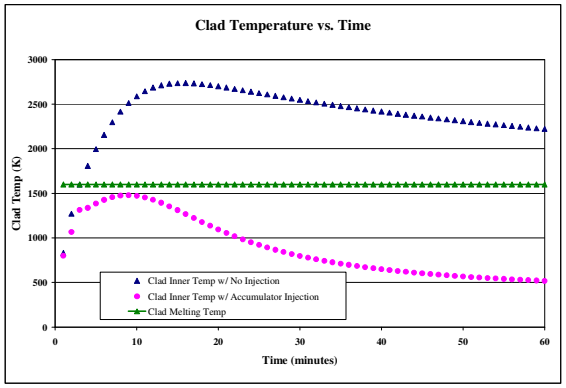

Fig. 5: Accumulator effect on cladding temperatures following LOCA

Technical Requirements for Neutron Source vis-à-vis Electric Power Production

The technical requirements for a tokamak fusion neutron source that would fulfill the transmutation mission are significantly less demanding than for an economically competitive tokamak electrical power reactor and somewhat less demanding than for a DEMO, as indicated in Table X.

TABLE X: Tokamak Neutron Source, Electric Power and DEMO Requirements

Parameter	**ITER**	**Transmutation**	**ElectricPower**[26]	**DEMO**[27]
Confinement $H_{IPB98}(y,2)$	1.0	1.0-1.1	1.5-2.0	1.5-2.0
Beta β_N	1.8	2.0-2.9	> 5.0	> 4.0
Power Amplification Q_p	5-10	3-5	> 25	> 10
Bootstrap Current Fraction f_{bs}		0.2-0.5	0.9	0.7
Neutron wall load (MW/m^2)	0.5	0.5-1.8	> 4.0	> 2.0
Fusion Power (MW)	410	200-500	3000	1000
Pulse length/duty factor	modest	long/steady-state	long/steady-state	long/steady-state
Availability (%)	<10	> 50	90	50

Conclusions

Sub-critical operation, with a neutron source, provides nuclear reactors with additional flexibility in achieving fuel cycles that better utilize fissionable material and that reduce long-lived transuranic isotopes in the material ultimately deposited in high-level-waste repositories, thus for realizing the ultimate objective of closing the nuclear fuel cycle. A tokamak D-T fusion neutron source based on ITER physics and technology, and for which ITER operation would serve as a prototype, would meet the needs of such transmutation reactors, thus enabling fusion to contribute to solving the world's energy and environmental problems at a much earlier stage than would be possible with pure fusion electricity production.

ACKNOWLEDGMENT The contributions of Profs. D. Tedder to fuel reprocessing, J. Lackey to nuclear fuels, C. de Oliveira to neutron transport calculations, J. Mandrekas and R. Johnson to plasma physics; the contributions of the fuel cycle theses of E. A. Hoffman and J. W. Maddox; and the conceptual design contributions of students in the Georgia Tech NRE design projects to the development of the material in this paper are gratefully acknowledged. This work was supported in part by DoE grant DE-FG0296ER54350.

REFERENCES

1. "First Phase P&T Systems Study: Status and Assessment Report on Actinide and Fission Product Partitioning and Transmutation", OECD/NEA, Paris (1999).
2. "Proc. 1st-5th NEA International Exchange Meetings", OECD/NEA, Paris (1990,92,94,96,98).
3. "Nuclear Wastes--Technologies for Separations and Transmutations", National Research Council, National Academy Press, Washington (1996).
4. "A Roadmap for Developing Accelerator Transmutation of Waste (ATW) Technology", US Dept. Energy report DOE/RW-0519 (1999).
5. AFCI websites http://www.nuclear.gov/afci and http://apt.lanl.gov.
6. GEN-IV roadmap website http://gif.inel.gov/roadmap/.

7. W. M. STACEY, "Capabilities of a DT Tokamak Fusion Neutron Source for Driving a Spent Nuclear Fuel Transmutation Reactor", *Nucl. Fusion, **41***, 135 (2001).
8. W. M. STACEY, J. MANDREKAS, E. A. HOFFMAN, et al., "A Fusion Transmutation of Waste Reactor", *Fusion Sci. Technol., **41***, 116 (2002).
9. A. N. MAUER, W. M. STACEY, J. MANDREKAS and E. A. HOFFMAN, "A Superconducting Fusion Transmutation of Waste Reactor", *Fusion Sci. Technol.,* **45**, 55 (2004).
10. J. MANDREKAS, L. A. COTTRILL, G. C. HAHN and W. M. STACEY, "An Advanced Tokamak Neutron Source for a Fusion Transmutation of Waste Reactor", Georgia Tech report GTFR-167 (2003).
11. W. M. STACEY, et al., "A Sub-Critical, Gas-Cooled Fast Transmutation Reactor (GCFTR) with a Fusion Neutron Source", *Nucl. Technol.*, **150**, 162 (2005).
12. W. M. STACEY, et al., "A Sub-Critical, He-Cooled, Fast Reactor for the Transmutation of Spent Nuclear Fuel", *Nucl. Technol.*, **156**, 99 (2006).
13. W. M. STACEY, et al., "Advances in the Sub-Critical, Gas-Cooled, Fast Transmutation Reactor Concept", *Nucl. Technol.*, (July, 2007).
14. E. A. HOFFMAN and W. M. STACEY, "Comparative Fuel Cycle Analysis of Critical and Subcritical Fast Reactor Transmutation Systems", *Nuclear Technol.*, **144**, 83 (2003).
15. E. A. HOFFMAN and W. M. STACEY, "Nuclear Design and Analysis of the Fusion Transmutation of Waste Reactor", *Fusion Sci. Technol.*, **45**, 51 (2004).
16. J. W. MADDOX and W. M. STACEY, "Fuel Cycle Anaysis of a Sub-Critical , Fast, He-Cooled Transmutation Reactor with a Fusion Neutron Source", *Nucl. Technol.*, 159, 94 (2007).
17. W.M. STACEY, J. MANDREKAS and E.A. HOFFMAN, "Sub-Critical Transmutation Reactors with Tokamak Fusion Neutron Sources", *Fusion Sci. Technol.*, **47**, 1210 (2005).
18. W. M. Stacey, "Transmutation Missions for Tokamak Fusion Neutron Sources", *Fusion Engr. Des.*, **82**, 11 (2006).
19. R. N. HILL and H. S. KHAHIL, "Physics Studies for Sodium Cooled ATW Blanket", Argonne National Lab report ANL/RAE/CP-105355 (2001).

20. F. H. SOUTHWORTH, et al., "The Next Generation Nuclear Plant (NGNP) Project", Proc. Global-3 Conf. (2003).
21. W. M. STACEY, *Fusion Plasma Physics*, Wiley-VCH, Berlin (2005), Ch. 19.
22. B. J. TOPPEL, "A User's Guide to the REBUS-3 Fuel Cycle Analysis Capability", ANL-83-2, Argonne National Laboratory (1983).
23. "ORIGEN-S: SCALE System Module to Calculate Fuel Depletion, Actinide Transmutation, Fission Product Buildup and Decay, and Associated Radiation Source Terms," NUREG/CR-200, Rev. & (ORNL/NUREG/CSD-2/V2/R7) Oak Ridge National Laboratory (2004).
24. W. M. STACEY, *Nuclear Reactor Physics*, Wiley-Interscience, New York (2001) Ch 2.
25. ARIES web site http://www-ferp.ucsd.edu/ARIES/.
26. W. M. STACEY "Tokamak Demonstration Reactors", *Nucl. Fusion*, **35**, 1369 (1995).